



HAL
open science

The Planck clusters in the LOFAR sky VI. LoTSS-DR2: Properties of radio relics

A. Jones, F. de Gasperin, V. Cuciti, A. Botteon, X. Zhang, F. Gastaldello, T. Shimwell, A. Simionescu, M. Rossetti, R. Cassano, et al.

► To cite this version:

A. Jones, F. de Gasperin, V. Cuciti, A. Botteon, X. Zhang, et al.. The Planck clusters in the LOFAR sky VI. LoTSS-DR2: Properties of radio relics. *Astronomy and Astrophysics - A&A*, 2023, 680, pp.A31. 10.1051/0004-6361/202245102 . hal-03982599

HAL Id: hal-03982599

<https://hal.science/hal-03982599>

Submitted on 5 May 2024

HAL is a multi-disciplinary open access archive for the deposit and dissemination of scientific research documents, whether they are published or not. The documents may come from teaching and research institutions in France or abroad, or from public or private research centers.

L'archive ouverte pluridisciplinaire **HAL**, est destinée au dépôt et à la diffusion de documents scientifiques de niveau recherche, publiés ou non, émanant des établissements d'enseignement et de recherche français ou étrangers, des laboratoires publics ou privés.



Distributed under a Creative Commons Attribution 4.0 International License

The *Planck* clusters in the LOFAR sky

VI. LoTSS-DR2: Properties of radio relics^{*}

A. Jones¹, F. de Gasperin^{2,1}, V. Cuciti¹, A. Botteon^{3,2,4}, X. Zhang^{4,5}, F. Gastaldello⁶, T. Shimwell^{7,4},
A. Simionescu^{5,4,8}, M. Rossetti⁶, R. Cassano², H. Akamatsu⁵, A. Bonafede^{3,2}, M. Brüggen¹, G. Brunetti²,
L. Camillini^{6,9}, G. Di Gennaro¹, A. Drabant¹⁰, D. N. Hoang¹, K. Rajpurohit^{3,2,10}, R. Natale^{6,9},
C. Tasse^{11,12}, and R. J. van Weeren⁴

¹ Hamburger Sternwarte, Universität Hamburg, Gojenbergsweg 112, 21029 Hamburg, Germany
e-mail: ajones@hs.uni-hamburg.de

² INAF – Istituto di Radioastronomia, via P. Gobetti 101, 40129 Bologna, Italy

³ DIFA – Università di Bologna, Via Gobetti 93/2, 40129 Bologna, Italy

⁴ Leiden Observatory, Leiden University, PO Box 9513, 2300 RA Leiden, The Netherlands

⁵ SRON Netherlands Institute for Space Research, Niels Bohrweg 4, 2333 CA Leiden, The Netherlands

⁶ INAF, IASF-Milano, via A. Corti 12, 20133 Milano, Italy

⁷ ASTRON, the Netherlands Institute for Radio Astronomy, Postbus 2, 7990 AA Dwingeloo, The Netherlands

⁸ Kavli Institute for the Physics and Mathematics of the Universe (WPI), The University of Tokyo, Kashiwa, Chiba 277-8583, Japan

⁹ Dipartimento di Fisica, Università degli Studi di Milano, Via Celoria 16, 20133 Milano, Italy

¹⁰ Thüringer Landessternwarte, Sternwarte 5, 07778 Tautenburg, Germany

¹¹ GEPI & USN, Observatoire de Paris, Université PSL, CNRS, 5 Place Jules Janssen, 92190 Meudon, France

¹² Department of Physics & Electronics, Rhodes University, PO Box 94, Grahamstown 6140, South Africa

Received 29 September 2022 / Accepted 5 December 2022

ABSTRACT

Context. It is well established that shock waves in the intracluster medium launched by galaxy cluster mergers can produce synchrotron emission, which is visible to us at radio frequencies as radio relics. However, the particle acceleration mechanism producing these relics is still not fully understood. It is also unclear how relics relate to radio halos, which trace merger-induced turbulence in the intracluster medium.

Aims. We aim to perform the first statistical analysis of radio relics in a mass-selected sample of galaxy clusters, using homogeneous observations.

Methods. We analysed all relics observed by the Low Frequency Array Two Metre Sky Survey Data Release 2 (LoTSS DR2) at 144 MHz, hosted by galaxy clusters in the second *Planck* catalogue of SZ sources (PSZ2). We measured and compared the relic properties in a uniform, unbiased way. In particular, we developed a method to describe the characteristic downstream width in a statistical manner. Additionally, we searched for differences between radio relic-hosting clusters with and without radio halos.

Results. We find that, in our sample, ~10% of galaxy clusters host at least one radio relic. We confirm previous findings, at higher frequencies, of a correlation between the relic-cluster centre distance and the longest linear size, as well as the radio relic power and cluster mass. However, our findings suggest that we are still missing a population of low-power relics. We also find that relics are wider than theoretically expected, even with optimistic downstream conditions. Finally, we do not find evidence of a single property that separates relic-hosting clusters with and without radio halos.

Key words. galaxies: clusters: general – galaxies: clusters: intracluster medium – radiation mechanisms: non-thermal – radiation mechanisms: thermal – catalogs

1. Introduction

Mergers of galaxy clusters generate shock waves that propagate through the intracluster medium (ICM). Since the characterisation of a cluster shock by Markevitch et al. (2002) with *Chandra*, many more have been found using measurements of the X-ray surface brightness, entropy, and temperature profiles of cluster outskirts (e.g., Ogrean & Brüggen 2013; Shimwell et al. 2015; Eckert et al. 2016; Akamatsu et al. 2017; Urdampilleta et al.

2018). The connection between radio relics (RRs) and merger shocks has been well-established by a number of shocks detected in X-rays, as ICM density and temperature discontinuities, at the location of a RR (e.g., Finoguenov et al. 2010; Bourdin et al. 2013; Akamatsu & Kawahara 2013; Botteon et al. 2016a,b). There is also clear evidence of the relation between RRs and galaxy cluster merger events from both weak lensing studies (e.g., Jee et al. 2016; Finner et al. 2017) and optical spectroscopy (e.g., Golovich et al. 2019). Not all RRs have a known associated shock, though this is likely the result of difficulties in shock detection from the low X-ray counts in cluster outskirts, where relics are typically located (Vazza et al. 2012; Ogrean et al. 2013). Fermi-I, diffusive shock acceleration (DSA)

* FITS images in Figs. A.1 and A.2 are available at the CDS via anonymous ftp to cdsarc.cds.unistra.fr (130.79.128.5) or via <https://cdsarc.cds.unistra.fr/viz-bin/cat/J/A+A/680/A31>

is typically adopted to explain the generation of RRs from cluster shocks (Enßlin et al. 1998). In DSA, charged particles are accelerated to relativistic energies by scattering upstream and downstream off magnetic inhomogeneities (Fermi 1949; Blandford & Eichler 1987). Due to the presence of cluster-scale magnetic fields, they emit synchrotron emission, which is observable as diffuse, roughly arc-like RRs (also known as cluster radio shocks, see Brunetti & Jones 2014; van Weeren et al. 2019, for reviews). The power-law energy spectrum of cosmic-ray electrons (CRes) produced by DSA generates a radio brightness profile in line with observations (e.g., Hoft & Brüggén 2007; Kang et al. 2012). Additionally, relics are typically observed to have high polarisation fractions ($\geq 20\%$ – 60%), matching expectations of magnetic field alignment along the shock surface (Enßlin et al. 1998). However, DSA from the thermal pool cannot entirely explain the properties of RRs. A study by Botteon et al. (2020a) found that acceleration of CRes from the thermal pool via DSA, in such weak shocks ($\mathcal{M} \lesssim 3$), is in most cases insufficient to explain the acceleration efficiencies required to produce the luminosity of relics. Re-acceleration of a pre-existing population of mildly relativistic CRes could relieve some of this tension (e.g., Markevitch et al. 2005; Kang & Ryu 2011; Pinzke et al. 2013). There is morphological and spectral evidence that the tails of radio galaxies can provide seed electrons that are re-accelerated by shocks (e.g., Bonafede et al. 2014; van Weeren et al. 2017; Di Gennaro et al. 2018). For example, van Weeren et al. (2017) found that the RR in Abell 3411-3412 is connected to the tail of a cluster-member radio galaxy. Moreover, the energy spectrum steepens along the tail, consistent with radiative losses, and subsequently flattens again at the inner boundary of the RR, implying re-acceleration. There are, however, still relatively few relics for which there is evidence of a connection/re-acceleration in general.

In addition to giant shock waves, galaxy cluster mergers generate turbulence in the ICM. This turbulence cascades down to smaller scales and can (re-)accelerate CRes and produce radio synchrotron emission, in the form of a radio halo (RH, see Brunetti & Jones 2014, for a review). These RRs are typically located in the cluster centre and follow the morphology of the X-ray-emitting gas. Numerous statistical studies of RRs have been performed and have shown a correlation between the RH power and its host cluster mass (e.g., Basu 2012; Cassano et al. 2013; van Weeren et al. 2021; Cuciti et al. 2021), as well as with the X-ray luminosity (e.g., Liang et al. 2000; Brunetti et al. 2009). In contrast, there have been relatively few statistical studies of RRs. Such investigations of relic properties are more challenging than for RRs due to a number of observational constraints. For example, the lower abundance of RRs (in $\sim 5\%$ of clusters, Kale et al. 2015), compared to that of RRs (in $\sim 40\%$ of clusters, e.g., Cuciti et al. 2021), and the typical location in the cluster periphery, where X-ray counts are low, make such studies challenging. Additionally, an unbiased measurement of the properties of relics is difficult, due to projection effects and their irregular morphologies. In the first statistical study of RRs, van Weeren et al. (2009) compiled all of those discovered (26 individual RRs) at that time from the literature. They discovered a correlation between the longest linear size (LLS) of a relic and its distance from the cluster centre. This finding was corroborated by de Gasperin et al. (2014; hereafter FdG14) and was found at low significance by Bonafede et al. (2012), who both restricted their analysis to only double radio relics (dRRs), that is to say pairs of diametrically opposed relics in the same cluster. The advantage of using dRRs is that the merger axis is relatively well-known and approximately on the plane

of the sky (van Weeren et al. 2011; Golovich et al. 2019), minimising projection effects. FdG14 also reported a correlation between host-cluster mass and RR power at 1.4 GHz, that is to say that more powerful relics are typically located in higher-mass clusters. However, simulations by Nuza et al. (2017) and Brüggén & Vazza (2020) suggest that we are missing a significant number of low-power relics, likely only detectable at low frequencies, and that the cluster mass provides a maximum radio power a relic can reach, rather than directly determining its power. The advent of sensitive, all-sky surveys at low radio frequencies will enable discovery of these low-power relics, if such a population exists.

In this paper we present the first statistical study of RRs at 150 MHz and their connection to RRs, using galaxy clusters covered by both the *Planck* PSZ2 catalogue (Planck Collaboration XXVII 2016) and the Low Frequency Array (LOFAR) Two Metre Sky Survey Data Release 2 (LoTSS DR2, Shimwell et al. 2022). Wherever possible, this was supplemented with archival *Chandra* and *XMM-Newton* data, to determine the X-ray properties of the sample clusters, which are described fully in Zhang et al. (2023). The biggest advantage of using such a sample is that it allows us to study RRs observed by the same telescope, and therefore approximately the same uv -coverage, observing frequency and sensitivity to compact and diffuse emission. Additionally, the observations were calibrated and the images produced in a uniform manner (see Tasse et al. 2021; Shimwell et al. 2022). The use of the PSZ2 catalogue allows us to produce a mass-selected sample, ensuring that our results are representative of those RRs observable at the sensitivity of LOFAR. This paper is the sixth in a series of papers¹ utilising the LoTSS DR2 – PSZ2 cluster sample to explore the properties of diffuse radio emission in the ICM. Botteon et al. (2022) describes the sample in detail, the methods and data used and the source classification. The occurrence and scaling relations of all RRs in this sample are presented in Cassano et al. (2023) and Cuciti et al. (2023), respectively, whilst upper limits on RH power in clusters with no detected diffuse emission are in Bruno et al. (2023). An analysis of the X-ray properties of the sample is presented in Zhang et al. (2023). See also Hoang et al. (2022) for analysis of diffuse radio emission within LoTSS DR2 in non-PSZ2 clusters.

The paper is structured as follows. Section 2 describes the sample of relics and how we measured their properties. In Sect. 3 we present our results. In Sects. 4 and 5 we discuss our results and conclude. We adopt a fiducial Λ CDM cosmology with $\Omega_{\Lambda} = 0.7$, $\Omega_{\text{m}} = 0.3$, and $H_0 = 70 \text{ km s}^{-1} \text{ Mpc}^{-1}$. All errors are at 1σ , unless otherwise stated.

2. The sample

We provide here a summary of the sample of relics used in this paper, its composition and the measurement of relic properties. For a full description of the cluster sample, including the data calibration, imaging procedure, and radio source classification, we refer the reader to Botteon et al. (2022).

2.1. Relics In LoTSS DR2

Of the 1653 galaxy clusters contained in the *Planck* PSZ2 catalogue (Planck Collaboration XXVII 2016), 309 lie within the LoTSS DR2 footprint (Shimwell et al. 2022). The LoTSS DR2 data were reprocessed to produce 144 MHz radio images, at

¹ https://lofar-surveys.org/planck_dr2.html

various resolutions, for each cluster (Botteon et al. 2022). The radio images were then visually inspected for evidence of diffuse emission not associated with an AGN. Elongated (≥ 300 kpc) diffuse emission with a sharp radio edge, lying outside the bulk of X-ray emission, in the cluster outskirts, was classified as a RR. Of those, relics diametrically opposed to another relic on the opposite side of its cluster were defined as dRRs. Some clusters host more than one RR, but do not fit this criterion and were therefore classified as multiple radio relics (mRRs). We use archival *Chandra* and *XMM-Newton* data to determine the cluster X-ray properties. The data are processed and used to produce images, smoothed to 30 kpc at the cluster redshift (see Botteon et al. 2022, for further details). A full analysis of the X-ray properties of the LoTSS DR2 – PSZ2 sample will follow in Zhang et al. (2023). For clusters with no *Chandra* or *XMM-Newton* observation, the emission was classified as a candidate radio relic (cRR), since it is not possible to define the location of the diffuse emission with respect to the ICM. In this case, the position of the radio emission with respect to the cluster optical overdensity was used. The resulting sample consists of 26 relic-hosting clusters, of which 20 have accompanying X-ray observations. Of the 35 individual relics residing in these clusters, 12 were defined as dRRs, 5 as mRRs and 6 as cRRs. The rest (12) were defined as RRs. There are no double, or multiple, candidate radio relics. For an image gallery of all RRs in our sample, and, where possible, their location with respect to the ICM X-ray emission, see Appendix A. Images and tables are taken from Botteon et al. (2022) and can be found at full resolution on the project website².

Radio halos in the LoTSS DR2 – PSZ2 sample were classified by Botteon et al. (2022). They were defined as extended radio sources occupying the same region as either the bulk ICM X-ray emission (RHs) or an overdensity of optical galaxies (cRHs). Of the 26 relic-hosting clusters, 12 also host a radio halo (11 RHs and 1 cRH). For some radio objects, originally classified as RHs, the low signal-to-noise ratio did not allow fitting of the model used to estimate RH flux (denoted RH*s/cRH*s, see Botteon et al. 2022, for more detail). We treated clusters which host such RH*s/cRH*s as hosting a RH, though there is only 1 relic-hosting cluster for which this is the case (PSZ2 G116.50-44.47, classified as RH*).

Figure 1 shows the mass distribution of all clusters in the LoTSS DR2 – PSZ2 sample, as a function of redshift, where the mass is M_{500} from the PSZ2 catalogue (Planck Collaboration XXVII 2016). Clusters which host at least one RR are shown as red points. PSZ2 G107.10+65.32 is comprised of two sub-clusters, each undergoing its own merger (Abell 1758, Botteon et al. 2020b). We have plotted this cluster separately, as a red star, since only the S sub-cluster hosts a RR, but, since the resolution of *Planck* is not sufficient to separate the two sources, the mass given in the PSZ2 catalogue is likely from a combination of the two sub-clusters. The blue dashed line shows the mass at which *Planck* is 50% complete, as a function of redshift. This line comes from converting the selection function from the *Planck* archive from SZ signal – cluster size to mass – redshift (Planck Collaboration XXVII 2016) and taking the boundary at which the probability of detecting a cluster is 50%. The only relic-hosting cluster which lies below this line is PSZ2 G069.39+68.05. Throughout this paper, we consider only clusters lying above this line as our representative cluster sample and restrict our analysis to only these clusters. However, since there is only one relic-hosting cluster below the

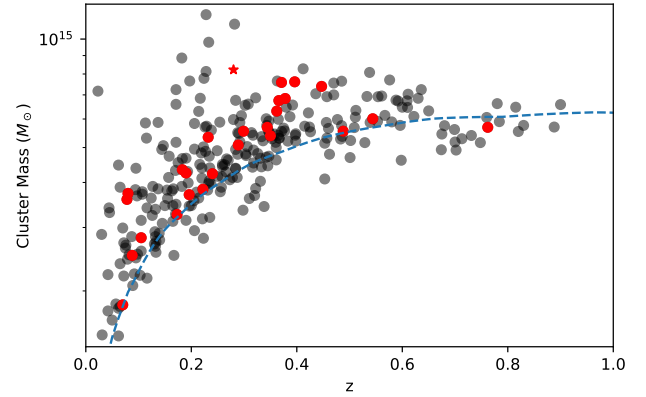


Fig. 1. Cluster M_{500} mass vs. redshift for all clusters in the LoTSS DR2 – PSZ2 sample. Red circles denote clusters which host at least one RR. Black circles denote all other clusters in the LoTSS DR2 – PSZ2 sample (Botteon et al. 2022). PSZ2 G107.10+65.32 S is plotted as a red star, since the mass reported in the PSZ2 catalogue likely comes from both sub-clusters, PSZ2 G107.10+65.32 N and PSZ2 G107.10+65.32 S. The 50% PSZ2 completeness line is shown in blue.

line (PSZ2 G069.39+68.05) and one for which we cannot be certain (PSZ2 G107.10+65.32), we plot these two relics whenever possible and label them accordingly, despite their absence from our analysis.

2.2. Relic measurements

All measurements used in this paper are presented in Botteon et al. (2022; Table A.4). For completeness, we describe the procedures used below.

Radio relics, owing to their often complex morphologies, do not lend themselves well to parametric model-fitting procedures, such as those used for RHs (Boxelaar et al. 2021). Connections of relics to radio galaxies, or even RHs, makes automatically separating relic from non-relic emission very challenging. Therefore, to best enable fair comparison of relic properties, we adopted a hybrid approach to their measurement. For each relic we manually defined a region which best covers it, whilst avoiding non-relic emission, by visually inspecting the radio and X-ray images. In general, we uniformly computed the properties of each relic from the 50 kpc-taper, compact-source-subtracted image of each cluster, where we defined relic emission as emission above $2\sigma_{\text{rms}}$ within the pre-defined region. σ_{rms} is the rms noise of the image. A few relics required slightly different treatment. The relics PSZ2 G089.52+62.34 N2 (Abell 1904), PSZ2 G091.79-27.00, PSZ2 G113.91-37.01 S, PSZ2 G166.62+42.13 E (Abell 746), and PSZ2 G205.90+73.76 N/S are not fully visible in the 50 kpc-taper images. We therefore chose to use the 100 kpc-taper images instead. Additionally, visual inspection of the model used to subtract compact sources in images of PSZ2 G190.61+66.46 revealed that it included some relic emission. Since there are no compact sources within the relic, we chose to use the 50 kpc-taper image without compact-source subtraction for this relic.

Figure 2 shows a reference image of PSZ2 G121.03+57.02, demonstrating the measurement of relic properties, as detailed below. The left panel shows the location of the relic, outside the bulk of ICM X-ray emission. The right panel shows a zoom-in of the relic from the 50 kpc-taper LOFAR image. The region used for this relic and the $\geq 2\sigma_{\text{rms}}$ contours are shown as white and black lines, respectively.

² https://lofar-surveys.org/planck_dr2.html

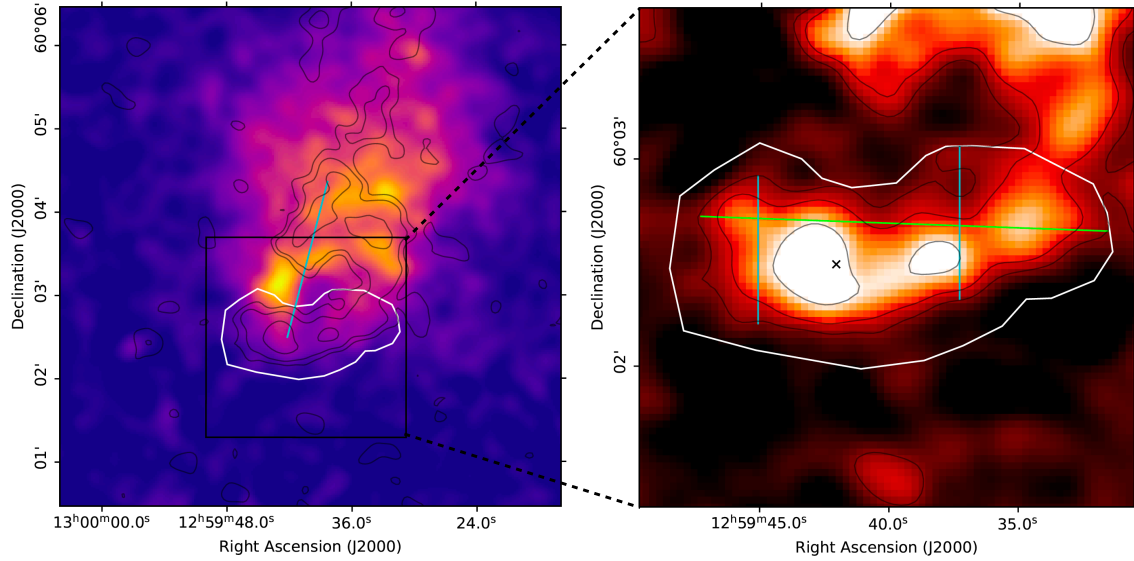


Fig. 2. Reference images of the relic in PSZ2 G121.03+57.02. The white region shows the region used to compute the properties of the relic. Black lines show the $2\sigma_{\text{rms}} \times [1, 2, 4, \dots]$ contours from the 50 kpc-taper, compact-source-subtracted LOFAR image from Botteon et al. (2022). *Left:* Chandra X-ray image. The cyan line scales the distance between the relic position and the cluster centre, as defined in Sect. 2.2. *Right:* zoom-in of the 50-kpc-taper, compact-source-subtracted LOFAR, centred on the relic. The green line shows the LLS of the relic. Two example lines used to measure the relic width are shown in cyan. The black cross is where we define the relic coordinate.

Since the LOFAR images are at a nominal frequency of 144 MHz, we computed the relic flux and power at 150 MHz, assuming $\alpha = -1$, where α is the spectral index ($S_\nu \propto \nu^\alpha$). The spectral index of RRs is typically in the range $-1 \lesssim \alpha \lesssim -1.5$ (e.g., Ferretti et al. 2012, FdG14). Since the frequency conversion is small and the clusters in our sample are relatively nearby, the choice of α in this range is somewhat arbitrary. If we instead choose $\alpha = -1.5$, corresponding to a steep-spectrum RR, the k -corrected 150 MHz RR power is $\lesssim 10\%$ greater, in most cases. Since the k -correction factor for a source with spectral index $\alpha = -1$ is zero, we did not need to k -correct our luminosities. The errors take into account a combination of the error from the rms noise and a 10% calibration error (Shimwell et al. 2022). We also included an error to account for residuals from the compact-source subtraction process. We split the images into four groups, based on their total discrete-source flux density, S_{discrete} , and assigned an appropriate fractional error which increases with S_{discrete} (see Botteon et al. 2022).

The LLS was calculated as the distance between the two pixels with maximum separation which were defined as part of the relic emission. Since the synthesised beam is the smallest angular scale across which we can trust the flux, the error in the LLS corresponds to one beam width. We used the same approach for all other distance measurements presented in this paper. We note that this can be considered a lower limit of the LLS, since we are limited by how much of the RR is detected. The LLS of PSZ2 G121.03+57.02 is shown in Fig. 2 as a green line.

Due to the often complex relic morphologies, the measurement of the relic extent downstream of the shock front, or relic width, is strongly dependent on the location at which it is measured. This makes it extremely difficult to measure a single width value in a consistent way which is fair for all relics in our sample. We therefore took a statistical approach, by measuring the width at many positions along the relic. In the case of a shock propagating outwards, the LLS should be oriented approximately perpendicular to the direction of propagation, that is perpendicular to the upstream – downstream direction. This orientation was

verified by eye, though we do not account for any curvature of the relic. We could therefore, at each pixel along the LLS, draw a line perpendicular to the LLS and calculate the maximum distance between relic pixels which lie on it. The blue lines in Fig. 2 (right) show two example lines used to calculate the width of the relic in PSZ2 G121.03+57.02. We then took the median of all values measured as the characteristic relic width and one standard deviation as its error. We chose to take the median as our characteristic width because it minimises the effect of small width measurements at the relic edges and areas with abnormally large widths. As with the LLS, the width measurements we made are lower limits, since the entire downstream extent of the RRs may be too faint to detect.

Without a direct detection of a shock front, it is not necessarily clear where the shock front producing a RR is located. There is still debate over the nature of the bright filaments often observed in RRs. However, a detailed, high-resolution study of the relics in Abell 3667 by de Gasperin et al. (2022) suggests that the filaments trace regions of shock acceleration. Recent simulations support the scenario that the brightest RR regions correspond to the highest Mach numbers (e.g., Domínguez-Fernández et al. 2021; Wittor et al. 2021). We therefore took the flux-weighted centre of the brightest 10% of relic pixels as the location of the RR. The coordinate calculated for PSZ2 G121.03+57.02 is shown as a black cross in Fig. 2 (right). We subsequently used this point to calculate the distance to the cluster centre, $D_{\text{RR}-c}$, where we considered the X-ray centroid of a cluster, measured within R_{500} , its centre (shown as black crosses in Fig. A.2) and to other relics, $D_{\text{RR}-\text{RR}}$, for dRRs. We note that, since the cRRs in our sample are those without accompanying X-ray images (see Sect. 2.1), we do not measure $D_{\text{RR}-c}$ for any cRRs. We included an additional error in these distance measurements to account for possible projection effects. The merger axes of dRR-hosting clusters are expected to lie on, or close to, the plane of the sky (van Weeren et al. 2011). We therefore set this additional error as the distance corresponding to a 10° offset. For all other relics, we use an offset of 30° .

3. Results

In this section, we report our results on the statistical properties of RRs and their host clusters. In general, throughout the figures, cRRs are denoted by triangular data points, dRRs by plusses, and all other relics, including mRRs, by circles. This notation extends to graphs with one data point per cluster, that is to say that clusters which host dRRs are plotted as a plus, etc.. Additionally, though not included in all graphs, data points with surrounding red circles denote clusters which also host an RH/cRH. Due to the ambiguity in PSZ2 G069.39+68.05 (below 50% *Planck* completeness, see Fig. 1) and PSZ2 G107.10+65.32 (double cluster, see Sect. 2.1 for more details), whenever possible, we label the points as ‘069’ and ‘107’ respectively, if they are included. We did not include these relics at all when plotting histograms, since they are not easily labelled. Since we did not include them when assessing the presence of a correlation, we also excluded them from the corresponding plots.

3.1. X-ray morphological disturbance

The dynamical state of the clusters in our sample is assessed using the 30 kpc-smoothed *Chandra* and *XMM-Newton* images. With these we are able to calculate the cluster concentration parameter (Santos et al. 2008),

$$c = \frac{F(r < R_{\text{core}})}{F(r < R_{\text{ap}})}, \quad (1)$$

where F is the X-ray flux, R_{core} the aperture of the core region and R_{ap} the outer aperture, and centroid shift (Mohr et al. 1993; Poole et al. 2006),

$$w = \left[\frac{1}{N_{\text{ap}} - 1} \sum_i (\Delta_i - \bar{\Delta})^2 \right]^{1/2} \frac{1}{R_{\text{ap}}}, \quad (2)$$

where N_{ap} is the number of apertures, Δ_i the centroid of the i th aperture, and $\bar{\Delta}$ the average centroid. R_{core} and R_{ap} were set following the convention of Cassano et al. (2010), that is 100 kpc and 500 kpc, respectively.

In Fig. 3 we plot the cluster concentration parameter, c against the centroid shift, w , for all clusters in the LoTSS DR2 – PSZ2 sample above the *Planck* 50% completeness line. The values, and corresponding errors, for all clusters are given in Botteon et al. (2022) and Zhang et al. (2023).

The plot shows the c and w parameters with their corresponding errors. We note that the combination of *Chandra* and *XMM-Newton* measurements and corresponding uncertainties, where available, gives rise to large errors in clusters where the two instruments disagree significantly. This is likely caused by differences in PSF and X-ray count rate between the two instruments. In general, however, there is good agreement of the concentration parameter and centroid shift between the two instruments (see Zhang et al. 2023, for a full discussion). However, there are no relic-hosting clusters which have large discrepancies between their *Chandra*-derived and *XMM-Newton*-derived morphological parameters. There is no clear bi-modal distribution representing disturbed and relaxed clusters, but, in general, clusters with smaller c and larger w are more dynamically disturbed. Relic-hosting clusters are shown in red, with all other clusters in black. We see that relic-hosting clusters primarily reside in the bottom right corner of the plot, corresponding to the most disturbed systems. Interestingly, the least disturbed cluster in the RR sample, PSZ2 G205.90+73.76, hosts both a RH and a dRR pair.

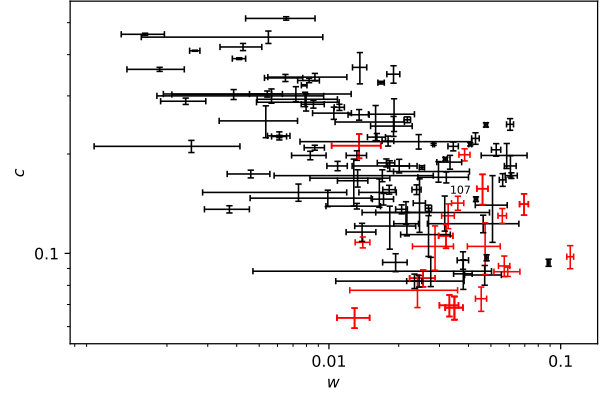


Fig. 3. Concentration parameter, c vs. centroid shift, w for all clusters with X-ray observations above the *Planck* 50% completeness line in the DR2 sample. Relic-hosting clusters are denoted by red points. All other clusters are black. PSZ2 G107.10+65.32 is labelled, with the label directly above the data point.

Cuciti et al. (2023) define a quantity, ‘disturbance’, using the c and w values of the clusters in our sample. This quantity has no physical meaning, but is useful to compare ‘disturbed’ and ‘relaxed’ clusters, since larger values correspond to more dynamically disturbed clusters. For clarity, we summarise its calculation here. We first normalised the values of c and w , to account for the different ranges covered by each, with

$$\mathcal{P}_{\text{norm}} = \frac{\log(\mathcal{P}_i) - \min(\log(\mathcal{P}))}{\max(\log(\mathcal{P})) - \min(\log(\mathcal{P}))}, \quad (3)$$

where \mathcal{P} represents either c or w . We then fit a line of the form $\log_{10}(c_{\text{norm}}) = m \log_{10}(w_{\text{norm}}) + q$ to the c_{norm} and w_{norm} data for all clusters with accompanying X-ray observations in the full LoTSS DR2 – PSZ2 sample. We derived the projected position of each cluster along this line and assumed that the cluster with X-ray disturbance = 0 is the first along the line starting from the top left corner of the plot. The disturbance of the other clusters was calculated as the distance along the same line from the cluster with disturbance = 0. We note that this quantity is similar to the relaxation score, \mathcal{R} , calculated by Zhang et al. (2023). Both quantities combine the two morphological parameters we have, c and w , into one, which describes the dynamical state of a cluster. The two quantities approximately anti-correlate, that is to say that lower \mathcal{R} is associated with higher values of disturbance. In our analysis, we chose to use the disturbance, since we remain consistent with the disturbance values for the RRs in the LoTSS DR2 – PSZ2 sample from Cuciti et al. (2023) and Cuciti et al. (2021). This disturbance represents the same information as the disturbance calculated by Cuciti et al. (2021), that is the logarithmic distance from the bisector of the median c and w values from Cassano et al. (2010) ($c = 0.2$, $w = 0.012$). The advantage of our method is that it does not rely on the somewhat arbitrary bisector slope and median c and w values. In Fig. 4 we plot the cluster disturbance distribution for all clusters above the *Planck* 50% completeness line in the LoTSS DR2 – PSZ2 sample with c and w measurements. The disturbance of all clusters is shown in grey, with all clusters hosting a RR in red. The clusters which host both a RR and a RH are shown by hatched black bars. As seen in the $c - w$ plot, relic-hosting clusters are among the most disturbed in our sample. There is no obvious difference between the disturbances of relic-hosting clusters which also host a RH and those that do not.

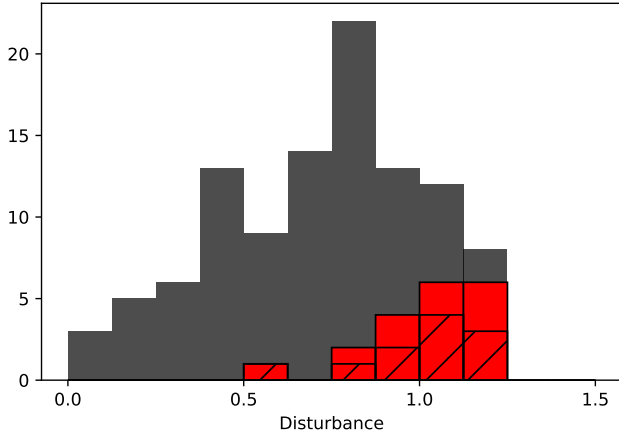


Fig. 4. Histogram of cluster disturbances. The grey bars show the distribution of all clusters above the *Planck* 50% completeness line in the LoTSS DR2 – PSZ2 sample with c and w measurements. The red bars show the distribution of all clusters which host a RR and the hatched bars show the clusters which host both a RR and RH. PSZ2 G107.10+65.32 is excluded entirely.

Table 1. Spearman rank correlation coefficient p -values for RR power – cluster mass, RR power – LLS, LLS – distance from cluster centre and LLS – distance from cluster centre as a fraction of R_{500} correlations.

Correlation	p -value	
	cRRs excluded	cRRs included
$P_{150\text{ MHz}} - M_{500}$	0.003	0.003
$P_{150\text{ MHz}} - \text{LLS}$	0.261	0.029
$\text{LLS} - D_{\text{RR}-c}$	0.002	–
$\text{LLS} - D_{\text{RR}-c}/R_{500}$	<0.001	–

Notes. The p -value is calculated separately with and without candidate relics included. There is no p -value including cRRs in the $\text{LLS} - D_{\text{RR}-c}$, nor the $\text{LLS} - D_{\text{RR}-c}/R_{500}$ correlation, since the distance from the cluster centre is computed using the cluster X-ray centroid. We note that PSZ2 G069.39+68.05 and PSZ2 G107.10+65.32 are not included in either sub-sample.

3.2. Radio relic scaling relations

For each of the relations reported in the following subsections, we calculated Spearman’s rank correlation coefficient and report its associated p -value. We assessed the presence of a correlation both including and excluding cRRs. PSZ2 G069.39+68.05 and PSZ2 G107.10+65.32 were excluded in both cases. The p -values for the correlations in the following subsections are reported in Table 1. We considered the null hypothesis to be rejected if $p < 0.05$, where the null hypothesis we are testing is that the variables X and Y are not correlated.

If the null hypothesis was rejected, we fit our data, using BCES linear regression methods (Akritas & Bershady 1996), to the equation $\log_{10}(X) = B \log_{10}(Y) + A$. This was done separately, both including and excluding the cRRs in our sample. We then calculated the 95% confidence interval of our line of best fit as

$$\Delta Y = \pm \sqrt{\left[\frac{\sum_{i=0}^N (Y_i - Y_m)^2}{N - 2} \right] \left[\frac{1}{N} + \frac{(X - X_m)^2}{\sum_{i=0}^N (X_i - X_m)^2} \right]}, \quad (4)$$

where $Y_m = B X_m + A$ and $X_m = \sum_{i=0}^N X_i / N$ for each observed X_i .

3.2.1. Radio power – cluster mass

Figure 5 shows the 150 MHz radio power of each relic in our sample against the host cluster mass (M_{500} , from *Planck*). The cluster redshift is shown on the colour bar. More massive relic-hosting clusters tend to be found at higher redshifts, due to the *Planck* cluster selection function (see Fig. 1). Low-mass clusters in our sample host only low-power RRs. Relics in more massive clusters span a larger range in radio power, but tend to host more powerful RRs than low-mass clusters. To quantify the scatter in the power distribution of RRs residing in high-mass ($>5.2 \times 10^{14} M_{\odot}$, where $5.2 \times 10^{14} M_{\odot}$ is the median cluster mass in our sample) and low-mass clusters ($\leq 5.2 \times 10^{14} M_{\odot}$), we calculate the coefficient of variance for each sub-sample. The coefficient of variance, defined as $c_v = \sigma/\mu$, where σ is the standard deviation and μ the mean, allows us to compare the scatter in two sub-samples with very different mean values. We find that in the high-mass bin, $c_v = 1.5$ and in the low-mass bin $c_v = 0.9$.

We find a positive correlation between the relic power and cluster mass ($p = 0.003$, both with, and without, cRRs). Table 2 shows the best-fit gradient (B) and y-intercept (A) values for the different fitting methods used, for the sample with and without cRRs included.

In Fig. 6 we plot the lines of best fit with (cyan dashed line) and without (black solid line) cRRs, from the orthogonal fit. The confidence interval, calculated using Eq. (4), is shown by the grey shaded region. We choose to plot the orthogonal-fit line, that is to say the line that minimises the orthogonal distances, as this is the same method used by FdG14 to compute their lines of best fit and enables fair comparison of the two relic studies. Their line of best fit is plotted as a dashed red line. For consistency, we plot the orthogonal-fit line for all other correlations in this paper.

The FdG14 sample selection is considerably different to ours. Their sample is comprised of all dRRs known at the time, in addition to the “elongated” relics of Feretti et al. (2012); 41 individual RRs, of which 30 are part of a dRR pair). The dRR-cluster sample of FdG14 contains only two clusters included in our sample, PSZ2 G071.21+28.86 (MACS J1752.0+4440) and PSZ2 G165.46+66.15 (Abell 1240). Additionally, PSZ2 G048.10+57.16 (Abell 2061) is also contained in the sample of Feretti et al. (2012). The cosmology used to calculate distances and luminosities (flat Λ CDM, $H_0 = 71 \text{ km s}^{-1} \text{ Mpc}^{-1}$, $\Omega_m = 0.27$) and the frequency (1.4 GHz) are both different to our sample. The cluster masses are also the M_{500} values given by *Planck*, though from the PSZ1 catalogue (Planck Collaboration XXIX 2014). The line, and corresponding red data points, were taken at a frequency of 1.4 GHz, so must be converted to 150 MHz, for comparison with our dataset. We do this using two slightly different approaches, shown in the top and bottom sections of Fig. 6. The first method (top) is to assume a constant spectral index, $\alpha = -1$, for all relics and scale the full FdG14 dataset and the line of best fit to 150 MHz uniformly. The advantage of using a constant spectral index to scale the FdG14 sample data is that we can also scale the line of best fit by the same factor, thereby allowing direct comparison of the slopes measured at both frequencies. We keep the original cosmology of the FdG14 data, since it was used to derive the line of best fit. Though the cosmology used for our dataset is slightly different to that used for FdG14, the results are almost identical (see Appendix B). Radio relics typically have spectral indices in the range $-1 \lesssim \alpha \lesssim -1.5$. Choosing the flattest spectrum in this range allows the closest comparison of the two samples, since even with this flatter spectral index, the RRs in our sample are, on average, less powerful. In this case, the slope of the line of best fit we obtain does not overlap with that

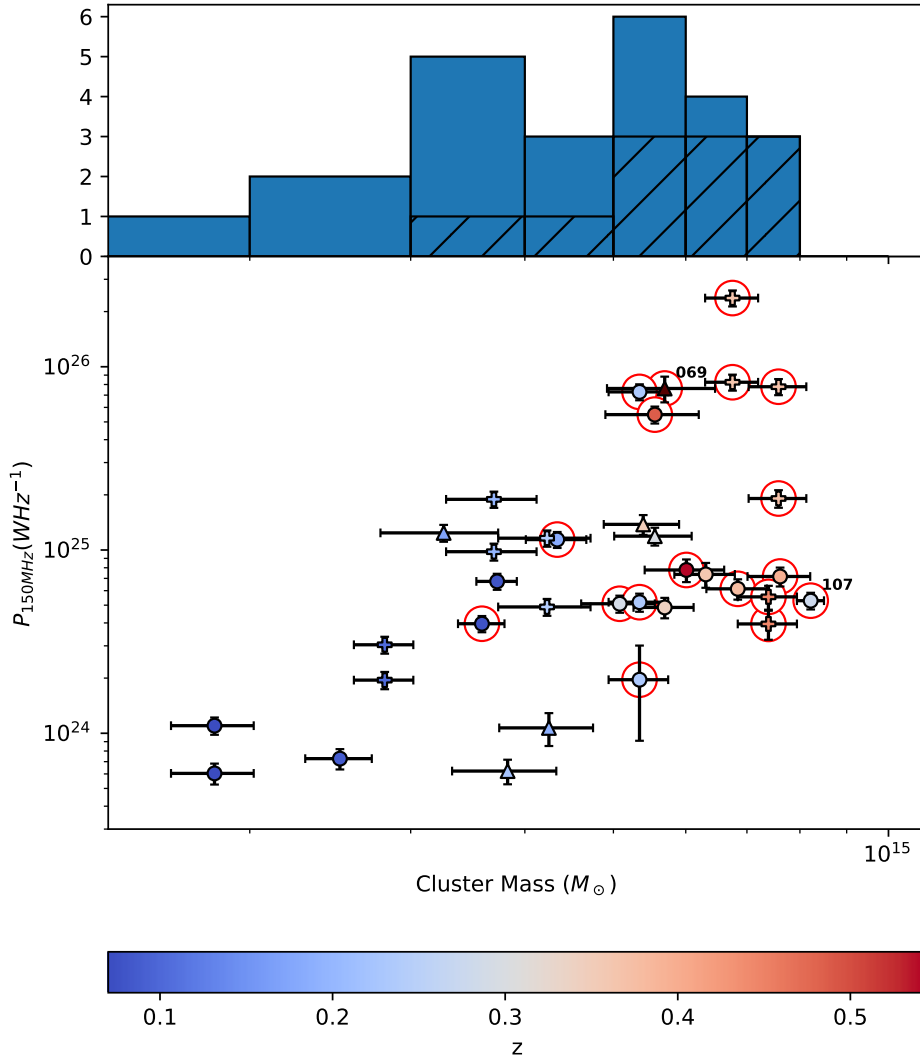


Fig. 5. Mass distribution of our RR sample. *Top:* as a histogram. The hatched bars show the distribution for only clusters which also host a RH. PSZ2 G069.39+68.05 and PSZ2 G107.10+65.32 are both excluded. *Bottom:* relic power vs. cluster mass with redshift on the colour bar. Triangles denote candidate relics and pluses those relics which are part of a double relic pair. All other relics are plotted as circles. Red circles surround relics in clusters which also host a RH. PSZ2 G069.39+68.05 and PSZ2 G107.10+65.32 are labelled, with the labels above and right of the data points.

of **FdG14** ($B_{\text{orth}} = 5.19 \pm 1.20$ vs. $B_{\text{fdg}} = 2.83 \pm 0.39$). The second rescaling method (bottom) is to use only the relics with measured spectral index in **FdG14** and scale each relic power by its actual spectral index. Since, in this case, the line of best fit reported by **FdG14** does not fit the rescaled data, we then recomputed the line of best fit (orthogonal method) ourselves. We obtained best-fit parameters of $B_{\text{fdg}} = 5.99 \pm 1.58$ and $A_{\text{fdg}} = -62.85 \pm 23.38$ for the rescaled **FdG14** data. We do not include any of our sample in the fitting procedure. In this case, the gradient of the line is within the errors of the line calculated for our sample. Qualitatively, we see that our dataset contains more low-mass clusters and more low-power relics in relatively high-mass systems, though it does not contain clusters as massive as in **FdG14**.

3.2.2. Radio power – LLS

We did not find a correlation between the power of RRs and their LLS, with cRRs excluded, that is to say we found that the null hypothesis could not be rejected ($p = 0.261$). However, when we included cRRs, we found that the null hypothesis was rejected ($p = 0.029$). Table 3 shows the best-fit gradient (B) and y-intercept (A) values for the different fitting methods used. Since the null hypothesis was only rejected when cRRs were included, we only calculated the best-fit parameters, A and B, for the entire sample. In Fig. 7 we plot the power against the relic LLS. The line

of best fit (orthogonal fit) is plotted as a dotted cyan line and its corresponding confidence interval the grey shaded region.

3.2.3. Longest linear size – cluster centre distance

We find that there is a positive correlation between the LLS of a relic and its distance from the cluster centre, $D_{\text{RR}-c}$, ($p = 0.002$) and its distance as a fraction of the cluster R_{500} ($p < 0.001$), that is to say larger relics are preferentially found further from the cluster centre. Table 4 shows the best-fit gradient (B) and y-intercept (A) values for the different fitting methods used. The slopes of both correlations are within errors for all fitting methods. We did not compute the Spearman rank correlation coefficient and perform fitting including cRRs, since we do not have any $D_{\text{RR}-c}$ or R_{500} measurements (see Sect. 2.2).

In Fig. 8 we plot the LLS of our relic sample against their projected distance from the cluster centre and as a fraction of the cluster R_{500} . The solid black line shows the orthogonal fit to our data, with its corresponding 95% confidence interval shown as the grey shaded region. The dashed red line shows the LLS – $D_{\text{RR}-c}$ correlation of **FdG14** ($B = 1.34 \pm 0.38$ and $A = -1.04 \pm 1.16$) for comparison. Both the gradients and intercepts of the regression lines for each sample are within the errors of each other. There is no LLS – $D_{\text{RR}-c}/R_{500}$ correlation in **FdG14** against which to compare. The colour bar denotes the

Table 2. Radio relic power – cluster mass line of best-fit parameters for different fitting methods.

Fit method	cRRs excluded		cRRs included	
	B	A	B	A
$Y X$	2.24 ± 0.44	-7.92 ± 6.46	2.30 ± 0.45	-8.94 ± 6.59
$X Y$	5.45 ± 1.25	-55.00 ± 18.32	6.11 ± 1.35	-64.70 ± 19.93
Bisector	3.22 ± 0.14	-22.37 ± 2.05	3.40 ± 0.15	-25.04 ± 2.13
Orthogonal	5.19 ± 1.20	-51.27 ± 17.60	5.84 ± 1.32	-60.84 ± 19.39

Notes. The parameters are calculated separately with and without candidate relics included. We note that PSZ2 G069.39+68.05 and PSZ2 G107.10+65.32 are not included in either sub-sample.

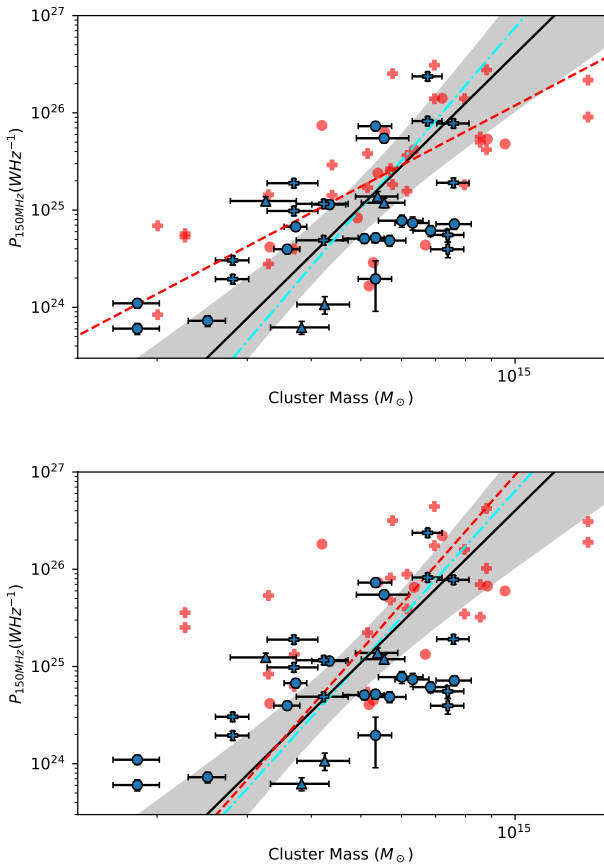


Fig. 6. Relic power vs. cluster mass with regression lines. Triangles denote candidate relics and pluses those relics which are part of a double relic pair. The black (solid) and cyan (dot-dash) lines are the orthogonal least squares regression lines for the relics in the DR2 sample. Black is if no candidate relics are included, with its corresponding confidence interval shaded, and cyan is if they are. Red points are the RRs from FdG14, with their corresponding regression line in red (orthogonal fit). Both PSZ2 G069.39+68.05 and PSZ2 G107.10+65.32 are excluded, since they are not used to calculate the regression lines. *Top:* FdG14 relic powers and regression line scaled to 150 MHz assuming $\alpha = -1$ for all relics. We note that the cosmologies used to calculate powers are slightly different between this sample data and the FdG14 data. See Fig. B.1. *Bottom:* FdG14 powers scaled to 150 MHz using the actual spectral indices of each relic. Relics with no spectral information in FdG14 are excluded. The regression line (orthogonal fit) is recomputed on the scaled data.

median relic width. We see, qualitatively, that larger relics typically have larger widths. It should however be noted that the errors on the width measurements are large, since we assigned

Table 3. Radio relic power – LLS line of best fit parameters for different fitting methods.

Fit method	B	A
$Y X$	1.23 ± 0.46	21.19 ± 1.36
$X Y$	8.28 ± 4.10	0.112 ± 12.32
Bisector	2.36 ± 0.19	17.82 ± 0.58
Orthogonal	7.60 ± 3.80	2.15 ± 11.42

Notes. The values quoted are only for cRRs included, since the null hypothesis was only rejected with their inclusion. PSZ2 G069.39+68.05 and PSZ2 G107.10+65.32 are not included.

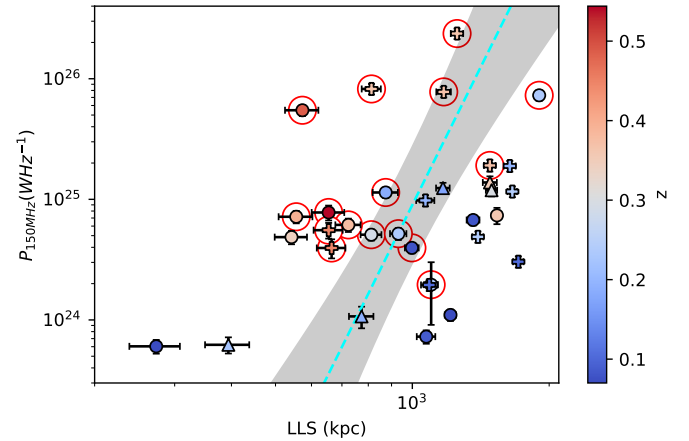


Fig. 7. Radio relic power vs. LLS. The host cluster redshift is on the colour bar. Triangles denote candidate relics and pluses those relics which are part of a double relic pair. All other relics are plotted as circles. Red circles surround relics in clusters which also host a RH. The dotted cyan line is the regression line (orthogonal fit) for our sample, including cRRs, with its corresponding confidence interval shaded. We note that there is no line of best fit excluding cRRs, since the null hypothesis could not be rejected in this case. Both PSZ2 G069.39+68.05 and PSZ2 G107.10+65.32 are excluded.

Table 4. Radio relic LLS – cluster-centre distance and LLS – cluster-centre distance as a fraction of R_{500} line of best fit parameters for different fitting methods.

Fit method	LLS – D_{RR-c}		LLS – D_{RR-c}/R_{500}	
	B	A	B	A
$Y X$	0.93 ± 0.21	0.14 ± 0.64	0.89 ± 0.21	2.97 ± 0.03
$X Y$	1.88 ± 0.38	-2.76 ± 1.16	1.96 ± 0.37	2.95 ± 0.04
Bisector	1.30 ± 0.13	-1.00 ± 0.38	1.29 ± 0.16	2.96 ± 0.03
Orthogonal	1.49 ± 0.27	-1.55 ± 0.82	1.50 ± 0.35	2.96 ± 0.03

Notes. PSZ2 G069.39+68.05 and PSZ2 G107.10+65.32 are not included.

the standard deviation of the width distribution measured as the error (see Sect. 2.2). For this reason, we did not perform a Spearman rank correlation coefficient test for any relic properties with the downstream width.

3.3. Relic – cluster centre distance

Figure 9 (top) shows the distribution of the projected RR-cluster centre distances, with a dashed (red) reference line at 800 kpc.

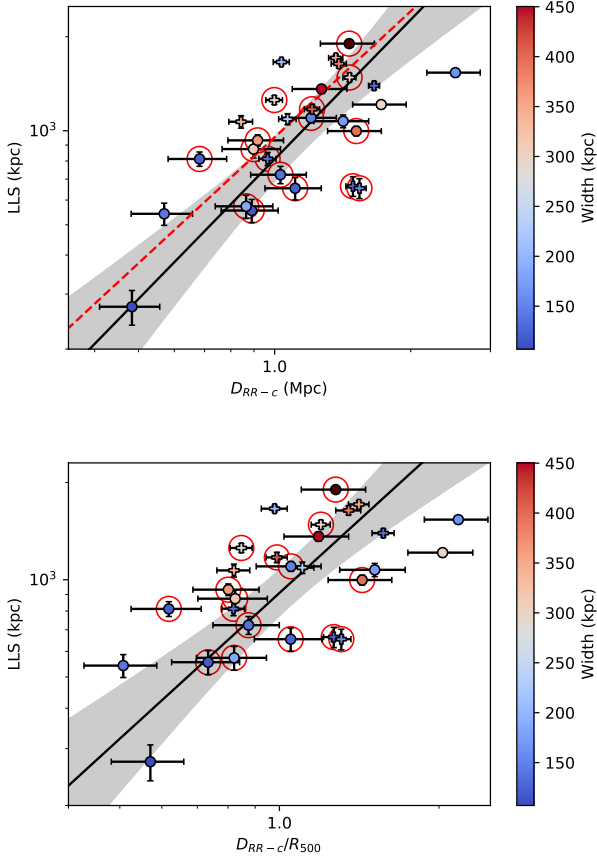


Fig. 8. Radio relic LLS as a function of its projected distance to the cluster centre. *Top*: LLS vs. cluster centre distance. The relic width is plotted on the colour bar. Pluses denote relics which are part of a double relic pair. All other relics are plotted as circles. Red circles surround relics in clusters which also host a RH. PSZ2 G107.10+65.32 is excluded. The black line is the regression line (orthogonal fit) for our sample, with its corresponding confidence interval shaded. The dashed red line is the regression line from FdG14. We note that there are no candidates, since the cluster centre is found from X-ray observations *Bottom*: same for the cluster centre distance as a fraction of the cluster R_{500} . There is no corresponding FdG14 correlation against which to compare.

The bottom panel shows the distribution as a fraction of R_{500} . The hatched bars show the distribution only for RH-hosting clusters. The solid and dashed black lines correspond to the median distances for all relics with D_{RR-c} measurements (except PSZ2 G107.10+65.32) and just those which also host a RH, respectively. The medians are very similar, in both cases and, in general, the distances of relics in RH-hosting clusters follow the distribution of the full sample relatively well. For simplicity, we exclude PSZ2 G107.10+65.32 from both plots entirely. PSZ2 G069.39+68.05 is automatically excluded, since it is a cRR-hosting cluster, and therefore has no D_{RR-c} or R_{500} measurements. Excluding PSZ2 G107.10+65.32, $25/28 = 89 \pm 19\%$ of the relics in our sample are >800 kpc from the cluster centre. For the sub-sample of RR-hosting clusters which also host a RH, this is $14/15 = 93 \pm 19\%$. One relic, in PSZ2 G091.79-27.00, is located 2.5 Mpc from its cluster centre, which is much further than for the other relics in our sample. $20/28 = 71 \pm 17\%$ of relics lie within the range $0.75 \leq D_{RR-c}/R_{500} \leq 1.5$. For RH-clusters in our sample, this becomes $14/15 = 93 \pm 19\%$. The relics PSZ2 G089.52+62.34 N2 and PSZ2 G091.79-27.00 are located $\geq 2R_{500}$ from their cluster centres.

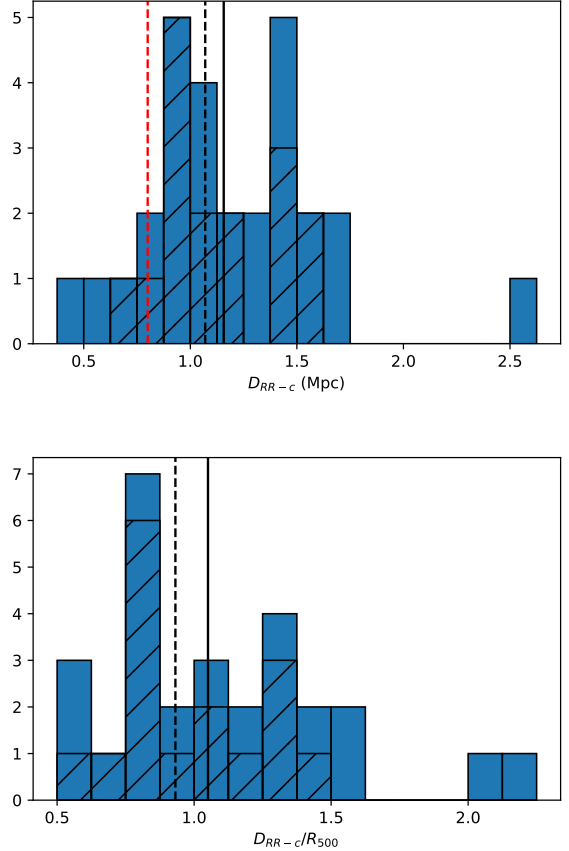


Fig. 9. Distribution of projected RR distances from their host-cluster centres. *Top*: histogram of the RR – cluster centre distances, D_{RR-c} . The red dashed line is at 800 kpc. *Bottom*: histogram of the RR – cluster centre distances as a fraction of the cluster R_{500} . The hatched bars show the distribution for only relics in RH-hosting clusters. The solid and dashed black lines correspond to the median distances for all relics and just those which also host a RH, respectively. We note that PSZ2 G107.10+65.32 is excluded for both histograms and the median calculations.

4. Discussion

4.1. Occurrence of RRs

Radio relics are relatively uncommon phenomena. Previous studies have found that $\sim 5\%$ of galaxy clusters host a RR (at 610/235 MHz, Kale et al. 2015). To calculate the RR occurrence at 150 MHz, we considered only clusters above the *Planck* 50% completeness line, except PSZ2 G107.10+65.32, since we do not know the mass of the relic-hosting, S subcluster (see Sect. 2.1). 273 of the 309 clusters in the full LoTSS DR2 – PSZ2 sample have adequate image quality to assess the presence of diffuse radio emission (see Botteon et al. 2022, for further details). Of these, 194 lie above the *Planck* 50% completeness line (excluding PSZ2 G107.10+65.32). In our sample, $19/194 = 10 \pm 6\%$ of galaxy clusters host at least one RR. If we also include all cRRs, we get that $24/194 = 12 \pm 7\%$ of clusters host at least one RR. We note that this is a soft lower limit at the sensitivity of LoTSS DR2, since there may be relics which are too faint to be detected with our observations. There are 42 clusters in the LoTSS DR2 – PSZ2 sample which contain diffuse radio emission of uncertain origin (classified as U in Botteon et al. 2022), but no RR or cRR classification. 33 of these lie above the *Planck* 50% completeness line. It is possible that some of these clusters also host RRs. However, it is unlikely that this would change our results

meaningfully, as, from visual inspection, a significant fraction of these appear to have a morphology more similar to RHs.

We assessed the effect of cluster mass on RR occurrence by splitting our sample into two mass bins: high ($>5.2 \times 10^{14} M_{\odot}$) and low ($\leq 5.2 \times 10^{14} M_{\odot}$), where $5.2 \times 10^{14} M_{\odot}$ is the median mass of our sample. We find that $10/89 = 11 \pm 7\%$ of high-mass clusters host at least one RR, which becomes $13/89 = 15 \pm 8\%$ when cRRs are included. For low-mass clusters, these occurrences are $9/105 = 9 \pm 6\%$ and $12/105 = 11 \pm 7\%$. The occurrences at high and low mass are within errors, suggesting that there is no dependence of the occurrence on the cluster mass, unlike for RHs (e.g., Cassano & Brunetti 2005; Cuciti et al. 2015, 2021).

Radio relics typically have steep spectra ($-1.0 \gtrsim \alpha \gtrsim -1.5$, e.g., FdG14, Feretti et al. 2012). The increase in relic occurrence at LOFAR frequencies, as compared to higher frequencies, is therefore unsurprising. Nuza et al. (2012) used the MARENOSTRUM UNIVERSE cosmological simulation to estimate the expected number of RRs that LOFAR would discover. By normalising the number of relics above a certain radio flux against the number of RRs observed at that point at 1.4 GHz, they predicted that LOFAR would discover ~ 2500 new relics, in $\sim 50\%$ of galaxy clusters. Even including cRRs and the relics in clusters below the *Planck* 50% completeness line, our sample contains only 35 RRs. If we extrapolate the number of relics detected in LoTSS DR2 to the entire northern sky, that is the area that will be covered upon the completion of LoTSS, we expect to observe 109 ± 58 RRs in the 835 PSZ2 detections that lie above 0° declination (see Botteon et al. 2022).

The absolute number of RRs observed is dependent on the underlying sample of galaxy clusters. The number of RRs predicted by Nuza et al. (2012) was not calculated using PSZ2 galaxy clusters, but rather on the X-ray NORAS+REFLEX sample. Additionally, Nuza et al. (2012) predicted that $>50\%$ of the relics detected by LOFAR would reside in clusters with $z > 0.5$. In the entire LoTSS DR2 – PSZ2 sample, only 46 clusters lie at such high redshift, and, of those, only 2 (including PSZ2 G069.39+68.05) host a RR. However, whilst not a complete study of all non-PSZ2 clusters covered by the LoTSS DR2 area, the results of Hoang et al. (2022) do not suggest that we are missing a large number of RRs because of our restriction to only PSZ2 clusters. Also, the fraction of clusters predicted to host RRs detectable by LOFAR is much greater than in our sample ($\sim 50\%$ vs. 10%). Therefore, unless the fraction of relic-hosting clusters varies significantly between the PSZ2 and NORAS+REFLEX samples, the number of relics able to be detected by LOFAR is significantly less than predicted by simulations.

One key assumption that governs the number of RRs observable is the efficiency of CRE acceleration by the shock. If the real acceleration efficiency is much lower than that assumed in simulations, the number of observable RRs will be overestimated, since the relic power is dependent on the efficiency ($dP(\nu)/d\nu \propto \xi_e$, where ξ_e is the fraction of kinetic energy dissipated at the shock, Hoeft & Brügggen 2007). Using the same cosmological simulation as Nuza et al. (2012), Araya-Melo et al. (2012) found that an acceleration efficiency of only $\xi_e = 0.0005$, that is to say a factor of ten lower than that assumed by Nuza et al. (2012), was sufficient to reproduce the NRAO VLA Sky Survey (NVSS) RR luminosity function.

An alternative cause of the discrepancy between simulations and the observed number of RRs could be the assumption of shock acceleration of electrons to relativistic energies from the thermal pool (standard DSA). Numerous studies have suggested

that re-acceleration of a pre-existing population of relativistic electrons is required to produce the observed brightness of RRs (e.g., Kang & Ryu 2011; Kang et al. 2012; Botteon et al. 2020a). Such a scenario relies on the existence of populations of mildly energetic electrons in the ICM available to be re-accelerated. The tails of radio galaxies could provide such a population, as has been suggested for Abell 3411-3412 (van Weeren et al. 2017). Another potential source is fossil plasma energised by ICM motions (e.g., de Gasperin et al. 2017; Mandal et al. 2020). Their ultra-steep spectra make such sources challenging to observe, so it is unclear how ubiquitous such populations are. If re-acceleration of relativistic electrons, instead of acceleration from the thermal pool, is required in some or all cases, many fewer RRs will be observed than predicted by simulations assuming standard DSA. This is because, in this scenario, only those shocks which cross a population of relativistic electrons will produce a RR.

4.2. Radio power of relics

In their statistical study of RRs, FdG14 found a positive correlation between the radio power of relics at 1.4 GHz and the mass of the host cluster, similar to that found for giant RHs (e.g., Basu 2012; Cassano et al. 2013; Cuciti et al. 2021). The physical explanation is that RRs are driven by shock waves caused by galaxy cluster mergers, for which the energy budget is set by the total mass of the merging clusters. The total energy released by a merger between two clusters of mass M and virial radius $R_{\text{vir}} \propto M^{1/3}$ is $E \propto M^2/R_{\text{vir}}$. Assuming that the kinetic energy dissipated at the shock is a fixed fraction of the total energy, and that it scales with the RR power, P , the power should scale like $P \propto E/t_{\text{cross}}$, where t_{cross} is the sound crossing time of the cluster and is related to the sound speed at the shock through $t_{\text{cross}} = R_{\text{vir}}/c_s$. X-ray studies show that cluster temperature, T , scales with $M^{2/3}$ (e.g., Pratt et al. 2009; Lovisari et al. 2020) and, since it also scales with c_s^2 , we would expect the radio power of relics to be related to the cluster mass by $P \propto M^{5/3}$.

For the first time, we show that the P – M correlation extends to frequencies below 200 MHz (see Sect. 3.2.1). However, we find that the relation is much steeper than that predicted by our simple estimate based on the total energy budget of the infalling mass, independent of the fitting method used (see Table 2). This could suggest that the assumption that a constant fraction of the total energy is dissipated at the shocks does not hold. Alternatively, it could suggest a dependence of the shock magnetic field or particle acceleration efficiency on the cluster mass. Additionally, observational bias may contribute to the measured slope of the P – M relation. We assess this effect in more detail in Sect. 4.2.1.

We also find a different mass dependency than that found by FdG14, who found that $P_{1.4\text{GHz}} \propto M^{2.8 \pm 0.4}$, whereas we find $P_{150\text{MHz}} \propto M^{5.2 \pm 1.2}$ using the same fitting procedure (orthogonal least squares). Figure 6 (top) shows the two correlations plotted on top of each other, with all data points and the correlation scaled to 150 MHz using a constant spectral index of $\alpha = -1$. Radio relics typically have spectral indices in the range $-1.0 > \alpha > -1.5$ (e.g., FdG14, Feretti et al. 2012). Even using the flattest spectrum within this range, we see that the majority of the relics in our sample lie below the correlation of FdG14. This is unsurprising, since RRs have relatively steep spectra. This, combined with the increased sensitivity of LOFAR and low operating frequencies, makes detection of low-power RRs easier. For a large number of relics in the FdG14 sample, spectral information is available. We therefore took all relics for which this is the

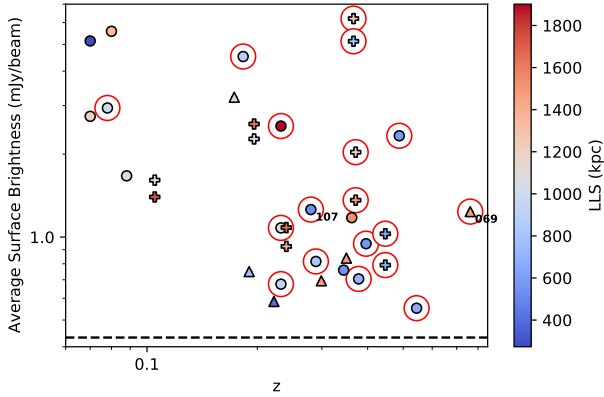


Fig. 10. Average relic surface brightness vs. redshift. The colour of the points shows the relic LLS. Triangles denote candidate relics and pluses those relics which are part of a double relic pair. All other relics are plotted as circles. Red circles surround relics in clusters which also host a RH. PSZ2 G069.39+68.05 and PSZ2 G107.10+65.32 are labelled, with the labels below and right of the data points. The dotted black line is at $2\sigma_{50\text{kpc}}$, where $\sigma_{50\text{kpc}} = 0.216 \text{ mJy beam}^{-1}$ is the average rms noise of the 50 kpc-tapered images in our sample.

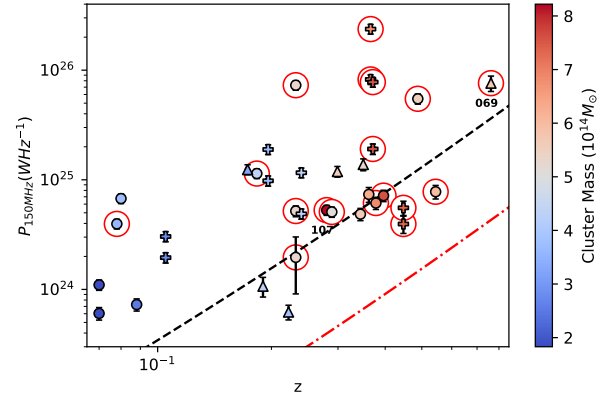


Fig. 11. Relic power vs. cluster redshift. The colour of the points shows the cluster mass. Pluses denote relics which are part of a double relic pair. All other relics are plotted as circles. Red circles surround relics in clusters which also host a RH. The black (dashed) and red (dot-dashed) lines show the estimated detection limit for the median ($\sim 1100 \text{ kpc} \times 200 \text{ kpc}$) and minimum ($\sim 300 \text{ kpc} \times 100 \text{ kpc}$) relic LLSs and widths of our sample, respectively. PSZ2 G069.39+68.05 and PSZ2 G107.10+65.32 are labelled, with the labels directly below the data points.

case, calculated the expected power at 150 MHz and recomputed the line of best fit on our re-scaled data (orthogonal fit). We note that this approach assumes no spectral curvature. The presence of which would cause the radio power at 150 MHz to be overestimated. The most detailed study of the integrated spectrum of a relic to-date however shows that the spectrum is straight (e.g., Rajpurohit et al. 2020). The re-scaled data, and its corresponding line of best fit, are plotted in Fig. 6 (bottom), along with the same line of best fit for the LoTSS DR2 – PSZ2 sample as before. We find that the lines of best fit are now remarkably similar, despite the greater number of low-power relics in our sample. These results suggest that taking the spectral index of each relic into account can entirely compensate for the discrepancy between the mass-dependence of each line of best fit.

4.2.1. Low-power RRs

If there exists a population of lower-power relics, especially at high redshifts, where most massive clusters are found, we may be unable to detect them. The power-mass correlation we measure would, in this case, be biased towards higher-power relics, since we only observe low-power RRs in nearby, low-mass clusters. Unlike for RHs, we do not have a robust method for determining upper limits for RRs in clusters defined as non-RR-hosting (e.g., Bonafede et al. 2017; Bruno et al. 2023). Instead, we must rely on simpler estimates from the typical noise of our observations. Figure 10 shows the surface brightness averaged across each relic as a function of cluster redshift. The black dashed line shows the approximate detection limit of our observations, given by two times the average rms noise of the 50 kpc-tapered images in our sample ($\sigma_{50\text{kpc}}$). Many of the higher-redshift relics lie just above the estimated detection limit.

We also assess this bias by estimating the radio power required for a RR to be observable, as a function of redshift. To do this we calculated the power of a box with dimensions of the minimum ($\sim 300 \text{ kpc} \times 100 \text{ kpc}$) relic LLS and widths of our sample and average surface brightness equal to $2\sigma_{50\text{kpc}}$ (as above), for a 50 kpc beam. This is shown as a red dot-dashed line in Fig. 11. Since we kept the beam at a fixed physical size, independent of redshift, the relic flux is constant. The least powerful,

high- z relics in our sample lie close to the $300 \text{ kpc} \times 100 \text{ kpc}$ line. Since the smallest relic (PSZ2 G089.52+62.34 N1, both smallest LLS and width) is considerably smaller than the other relics in our sample (see Fig. 8), we also calculated the same sensitivity limit for the average relic. The box dimensions were, in this case, the median LLS and width values of our sample ($\sim 1100 \text{ kpc}$ and 200 kpc). This is plotted as a dashed black line in Fig. 11. A few relics lie between the two sensitivity lines, but most lie above the median line. As in FdG14, we find that the faintest relics we observe are at the detection limit of our observations. This implies that the missing low-power relic population might just be a selection effect.

Additionally, the least powerful relics are found only in nearby clusters. Of the 7 relics with radio powers $< 3 \times 10^{24} \text{ WHz}^{-1}$ (PSZ2 G080.16+57.65, PSZ2 G086.58+73.11, PSZ2 G089.52+62.34 N2, PSZ2 G089.52+62.34 N1, PSZ2 G099.48+55.60 S, PSZ2 G144.99-24.64, PSZ2 G166.62+42.13 E), all are located at $z < 0.25$. This is unsurprising, since, for a given power, the flux observed decreases with distance. However, since in our sample more massive clusters are generally located at higher redshifts (see Fig. 1), this effectively places an approximate lower limit on the power detectable with LOFAR at a given cluster mass. If we take the approximate sensitivity limit calculated for an average relic in our sample (Fig. 11, black dashed line), we would expect that a relic with radio power $3 \times 10^{24} \text{ WHz}^{-1}$ would be too faint to be observable in LoTSS DR2 if it were located $z \gtrsim 0.27$. Comparing the masses of the clusters in our sample located above and below this redshift, we find that the median mass above ($6.2 \times 10^{14} M_{\odot}$, from 14 clusters) is much greater than below ($3.7 \times 10^{14} M_{\odot}$, from 12 clusters). This implies that if such a population of low-power RRs also exists at high redshift, and therefore mass, we would be unable to detect them.

Studies focussing on the properties of large samples of simulated RRs (e.g., Nuza et al. 2017; Brüggén & Vazza 2020) suggest that there is a large number of low-power RRs, especially in low-mass clusters. The low-mass systems in our sample are among the least massive clusters known to host RRs, with only the relics in Abell 168 being hosted by a lower-mass cluster

($M_{500} = 1.2 \times 10^{14} M_{\odot}$ from the X-ray mass – luminosity correlation, Piffaretti et al. 2011; Dwarakanath et al. 2018) than PSZ2 G089.52+62.34 ($M_{500} = 1.8 \times 10^{14} M_{\odot}$) in our sample. LOFAR has allowed for the discovery of relics in low-mass clusters, such as in PSZ2 G145.92-12.53 ($M_{500} = 1.9 \times 10^{14} M_{\odot}$ from PSZ2, Botteon et al. 2021). In fact, of the 11 clusters $< 5 \times 10^{14} M_{\odot}$ in our sample, the RRs in nine of them were discovered for the first time with LOFAR, or in combination with another instrument. The low-mass end of our sample is nonetheless sparsely populated. Our results suggest that we could well be missing a number of low-power RRs, especially in low-mass clusters. This would appear to weaken the finding of a correlation between cluster mass and the power of a RR and may suggest that, in contrast to RHs, the merging mass is not a direct driver of the relic power, as suggested by Nuza et al. (2017). However, it should be noted that the discrepancy between observed and simulated relic counts (see Sect. 4.1) cast doubt on the existence of a large population of undetected relics and suggest that cosmological simulations are unable to fully produce the observed RR population properties. Indeed, this would support the idea that the cluster mass sets an approximate upper limit on the power of a relic, but additional factors drive the differences in observed brightness. For example, the particle acceleration efficiency is a function of the underlying shock Mach number (Hoeft & Brüggén 2007) and could therefore drive differences in RR power. Additionally, if relics are produced by re-acceleration of mildly relativistic fossil electrons, the properties of the electron population would also affect the power of the relic.

4.2.2. On the scatter in the power-mass correlation

Cuciti et al. (2021) found that the scatter in the $P_{150\text{MHz}} - M_{500}$ for giant RHs can be, at least in part, explained by the morphological cluster disturbance. Radio halos that lie above the correlation tend to be found in more disturbed clusters. We investigate whether this can also explain the scatter for the $P_{150\text{MHz}} - M_{500}$ correlation for relics. We calculated the error in the distance from the correlation with bootstrapping methods. We assigned the cluster mass and radio power of each relic a random number drawn from a Gaussian distribution with mean of the measured value and standard deviation the corresponding errors. We then re-fitted the data with an orthogonal fit and measured the distance of each point from the new correlation. This was repeated 1000 times and we use the standard deviation of the distance measurements as the random error. The total error is from a combination of this error and the power error of each relic.

In Fig. 12 (top) we plot the logarithmic distance, along the $P_{150\text{MHz}}$ axis, of a RR from the $P_{150\text{MHz}} - M_{500}$ correlation for all relics (orthogonal fit) against the cluster disturbance (see Sect. 3.1). As the lines of best fit including, and excluding, cRRs (see Table 2) are so similar, we use the line of best fit including cRRs. We do not find a correlation between the disturbance and the distance from the correlation. In Fig. 12 (bottom) we plot the distance from the same correlation against the relic LLS. Smaller relics tend to lie below the $P_{150\text{MHz}} - M_{500}$ correlation and larger relics above. This finding is expected, since for a given surface brightness, a larger relic should be more powerful. The correlation found between the RR power and the LLS supports this (see Sect. 3.2.2), although this correlation is only found when cRRs are included. The smallest relic (PSZ2 G089.52+62.34 N1) is an outlier, in that it is a very small relic (~ 300 kpc) which lies well above the correlation. This relic is connected, at least in projection, to an AGN (see van Weeren et al. 2021, for more details), which could

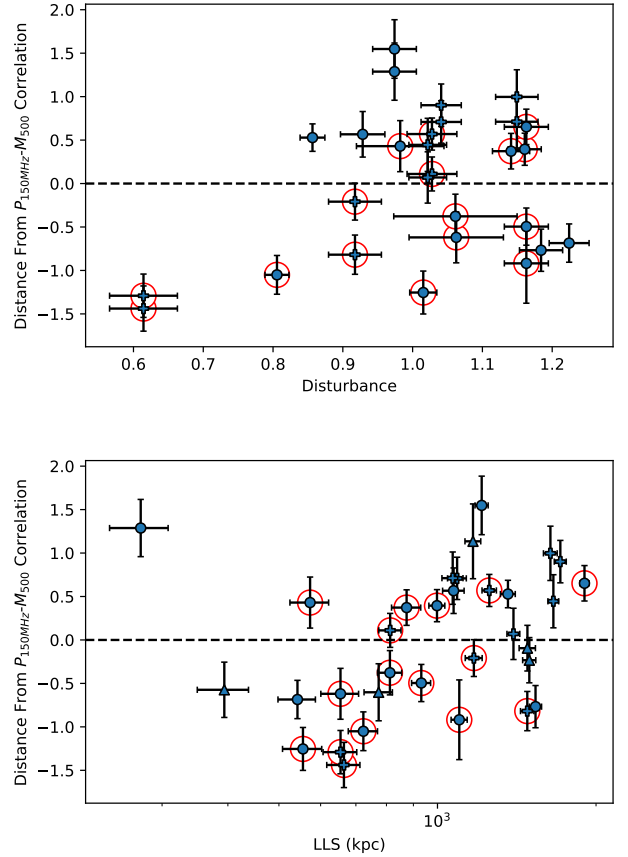


Fig. 12. Logarithmic distance from $P-M$ correlation (along $P_{150\text{MHz}}$ axis, Fig. 6) vs. LLS (*top*), disturbance (*bottom*). The distance is calculated from the orthogonal fit on all relics (except PSZ2 G069.39+68.05, PSZ2 G107.10+65.32; see Table 2). PSZ2 G069.39+68.05, PSZ2 G107.10+65.32 are excluded from the plots.

have had an effect on the relic’s brightness. Such an effect has been observed in other relics, such as PSZ2 G096.88+24.18 (Jones et al. 2021). However, PSZ2 G089.52+62.34 is also a low-mass cluster, where we observe very few relics and therefore the correlation is poorly constrained.

4.3. Downstream relic width

The downstream width of a RR is set by the radiative lifetime of the CRes producing the relic. In the case of DSA, electrons at a shock front in the ICM are (re-)accelerated to relativistic energies. However, as the shock propagates through the ICM, in the absence of another acceleration mechanism, the electrons left behind the shock lose energy through inverse Compton (IC) and synchrotron emission until they become too faint to observe. For some relics, there is evidence that the downstream width is too large to be fully explained in this scenario. By estimating the expected width of a relic, given synchrotron and IC losses, Kang et al. (2017) found a discrepancy of a factor of ~ 2 in the Toothbrush relic at 610 MHz. The effect is particularly pronounced at low radio frequencies however. Performing similar estimations, de Gasperin et al. (2020) found that the width of the relic was ~ 4 times larger than predicted at 58 MHz. A similar discrepancy was found for the Sausage relic (Kang 2016) and in Abell 3667 (de Gasperin et al. 2022).

For the first time, we systematically measure the downstream widths of relics, by calculating the width at many points along

the relic to produce a distribution of widths (see Sect. 2.2). Figure 13 shows the medians of the measured relic width distributions as a function of redshift. The error bars correspond to the standard deviation of the width distributions. To compare our width measurements against theoretical expectations, we use Kang et al. (2017, Eq. (1)), who estimated the characteristic downstream width behind a spherical shock at a given frequency, due to IC and synchrotron losses. The width is then given by

$$\Delta l_\nu \approx 120 \text{ kpc} \left(\frac{u_{\text{down}}}{10^3 \text{ kms}^{-1}} \right) \cdot Q \cdot \left[\frac{\nu_{\text{obs}}(1+z)}{0.61 \text{ GHz}} \right]^{\frac{1}{2}}, \quad (5)$$

where u_{down} is the downstream shock speed, ν_{obs} is the observing frequency, and Q depends on the downstream magnetic field, B_{down} , as

$$Q \equiv \left[\frac{(5 \mu\text{G})^2}{B_{\text{down}}^2 + B_{\text{CMB}}^2} \right] \left(\frac{B_{\text{down}}}{5 \mu\text{G}} \right)^{\frac{1}{2}}, \quad (6)$$

where $B_{\text{CMB}} = 3.24(1+z)^2 \mu\text{G}$ is the equivalent magnetic field strength of the cosmic microwave background (CMB). Since we do not have information on the downstream magnetic field strength, we assumed the magnetic field strength which minimises radiative losses, that is $B_{\text{down}} = B_{\text{CMB}}/\sqrt{3}$. The theoretical widths we calculated therefore correspond to the maximum expected width. The expected width is also strongly dependent on the downstream flow speed, u_{down} , which depends on the shock Mach number, \mathcal{M} , and upstream sound speed, $c_{\text{s,up}}$. $c_{\text{s,up}}$ is then related to the downstream sound speed, $c_{\text{s,down}}$,

$$\text{by } c_{\text{s,down}}/c_{\text{s,up}} = \sqrt{\frac{(5\mathcal{M}^2 - 1)(\mathcal{M}^2 + 3)}{16\mathcal{M}^2}}. \text{ We estimated } u_{\text{down}},$$

using $u_{\text{down}} = c_{\text{s,up}} \frac{\mathcal{M}^2 + 3}{4\mathcal{M}}$, and $c_{\text{s,down}} \approx 1480 \text{ kms}^{-1} \left(\frac{T_d}{10^8 \text{ K}} \right)^{1/2}$. By assuming a number of reasonable \mathcal{M} , and downstream temperatures, T_d , we could therefore estimate the maximum expected relic width. The resulting expected widths are plotted in Fig. 13. The maximum downstream speed reached with these parameters is $\sim 10^3 \text{ kms}^{-1}$. Only PSZ2 G089.52+62.34 N1, the smallest relic in our sample, lies completely below the uppermost line. The widest relic (PSZ2 G166.62+42.13 W, median width $\sim 700 \text{ kpc}$) would require $u_{\text{down}} \sim 5000 \text{ kms}^{-1}$ to agree with the prediction.

Clearly, the width of RRs is greater than expectations in almost all cases, for our sample. In most cases, even optimistic assumptions of the downstream temperature and Mach number are insufficient to explain the median values of our calculated width distributions. One possible solution to this is that downstream turbulence further accelerates the relic-producing CRes, extending their radiative lifetime (e.g., Fujita et al. 2016). Evidence of turbulence in the downstream regions of relics has been discovered in some clusters. For example, Kale et al. (2012) and Jones et al. (2021) found patchy polarised emission in the Abell 3376 and PSZ2 G096.88+24.18 relics, respectively, which they each attributed to turbulence. Di Gennaro et al. (2021) performed an extensive analysis of the polarisation structure in the Sausage relic using RM-synthesis. They found that the observed depolarisation could be explained by a turbulent magnetic field strength of $B_{\text{turb}} \sim 5.6 \mu\text{G}$. Simulations of the Sausage and Toothbrush relics, by Kang (2016) and Kang et al. (2017) respectively, found that they could be explained by shock re-acceleration of fossil electrons with post-shock turbulence. It is not clear if this can explain the systematic offset between the expected and observed relic widths, since the downstream region of only a few relics show indications of turbulence. Another possibility is that, in general, the shock is broken and complex in

shape, so multiple shocks can travel one after the other, artificially expanding the post-shock region. This is a proposed scenario to explain the filaments in Abell 3667 (de Gasperin et al. 2022), and many other RRs show a complex, filamentary sub-structure (e.g., George et al. 2015; Di Gennaro et al. 2018; Rajpurohit et al. 2022).

4.4. Radio halos in relic-hosting clusters

The connection between galaxy cluster mergers and both RRs and giant RHs is well-established. It is however unclear why, in addition to clusters which host both RR(s) and RH(s), there are numerous clusters which only host one or the other. In a study of dRR-hosting clusters, Bonafede et al. (2017) investigated the differences between clusters with and without RHs. In their work, they found no relation between the merger mass ratio and the presence of RHs. However, they did find a possible relation with the time since merger, though the statistics were too low to be conclusive.

In our sample, only 6 clusters host dRRs and, of these, 3 also host a giant RH. The statistics are therefore much too low to limit our analysis to only dRRs. If the difference between RH-hosting and RR-hosting clusters is evolutionary, that is to say that they are produced at different times over the course of a merger, we might expect that there is a characteristic time since merger when RHs are produced. MHD simulations of two clusters by Donnert et al. (2013) support this scenario. They found that the power of the RHs produced evolved throughout the merger from radio-quiet during the infall phase, to radio-loud as turbulence is driven throughout much of the cluster volume and finally decays to become radio-quiet again. Using the distance between a relic and the cluster centre as a proxy for the time since merger, we can investigate such an effect. In Fig. 9 we plot histograms of the distance of the relics to the cluster centre and the distance as a fraction of the cluster R_{500} . The black, hatched bars show those relics which are in RH-hosting clusters. There is no clear distinction in the relic distance, nor as a fraction of cluster R_{500} , between clusters with and without RHs. The distribution of relics in RH-hosting clusters is similar to those without, though at the most extreme distances none of the clusters also host a RH. The statistics are low, but this is similar to the results of Bonafede et al. (2017), where clusters with a giant RH occupied the centre of the time-since-merger distribution. They suggested that, in early mergers, turbulence has not had enough time to cascade down to scales at which particles can be (re-)accelerated and, in late mergers, the CRes producing RHs may have already become too faint to observe, due to IC and synchrotron losses. Relics on the other hand, due to continued shock acceleration, would be able to stay visible for longer. Though this assumes that the shock passage lasts longer than the timescale of turbulence able to produce RHs. In their study on the observed fraction of RHs in merging galaxy clusters, Cassano et al. (2016) found that the absence of RHs in some merging clusters could be explained by an RH-lifetime of $\sim (0.7-0.8)\tau_{\text{merger}}$, where τ_{merger} is the merger timescale. If RRs have longer lifetimes, this may go some way to explaining the difference between RH-hosting and RR-hosting clusters, though this would not explain why many clusters are observed with RHs but not RRs. Cassano et al. (2016) also found evidence that RHs may instead be produced only in larger mass ratio merger events. If RR generation has a different dependence on the mass ratio, this could also contribute to the discrepancy we observe. Unfortunately, we do not have data on the merging mass ratio for our sample and are therefore unable to investigate the effect.

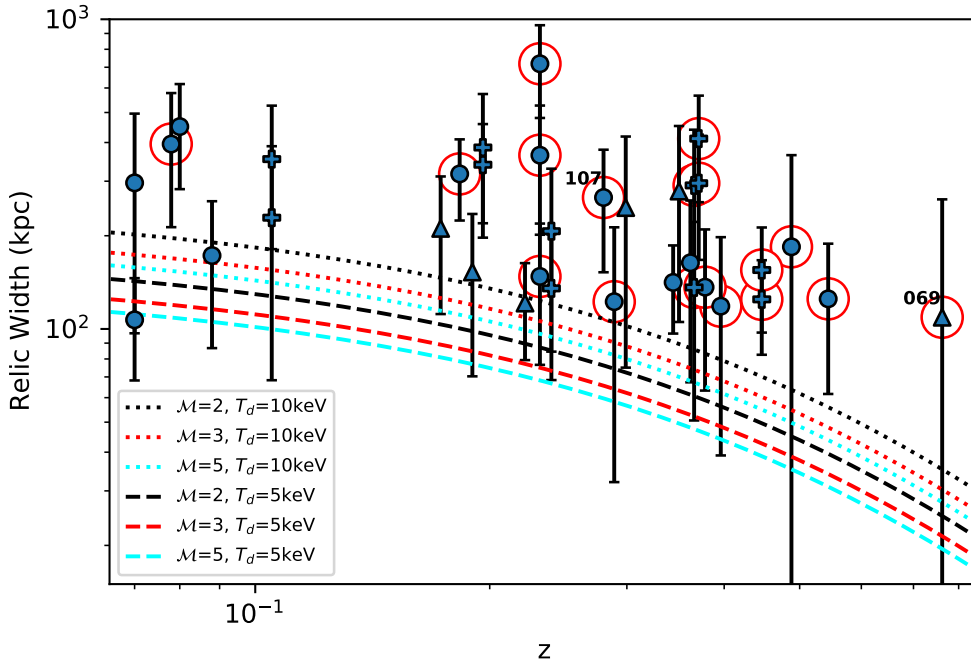


Fig. 13. Median relic width vs. redshift. The error bars correspond to the standard deviation of the relic widths measured. Triangles denote candidate relics and pluses those relics which are part of a double relic pair. All other relics are plotted as circles. Red circles surround relics in clusters which also host a RH. The dashed and dotted lines show the largest expected relic width from Kang et al. (2017) for different shock properties. PSZ2 G069.39+68.05 and PSZ2 G107.10+65.32 are labelled, with the labels above and left of the data points.

Another possibility is that the difference between the two populations is due to the merging state. Turbulence is injected into the ICM directly by the merger. Minor mergers may therefore be unable to inject enough turbulence into the ICM to produce visible RHs (Cassano & Brunetti 2005). If this were the case, we might expect that clusters with both relics and halos are more morphologically disturbed than those with only relics. From Figs. 3 (bottom) and 4 we see however that clusters with both populate the same regions as those with only relics. Furthermore, the least morphologically disturbed cluster (PSZ2 G205.90+73.76) hosts a dRR and a RH.

In almost all plots we include red circles to denote clusters hosting both a RH and relic(s), and see no clear distinction between the two populations in any, except in the $P_{150\text{MHz}} - M_{500}$ plot (Fig. 5). In this plot, we see a clear split in the number of halos in relic-hosting clusters between low-mass and high-mass clusters. The histogram in Fig. 5 shows the mass distribution of clusters in our sample. The hatched bars show the distribution for only clusters which also host a RH. Of the 19 clusters which host at least one relic, $11/19 = 58 \pm 15\%$ also host a RH. Including cRRs, this becomes $11/24 = 46 \pm 14\%$, as no cRR-hosting cluster also hosts a cRH³. The number of RH increases sharply with cluster mass. The fraction of relic-hosting clusters below the median cluster mass, $5.2 \times 10^{14} M_{\odot}$, which also host an RH, is $3/9 = 33 \pm 12\%$, of which none are below $3.5 \times 10^{14} M_{\odot}$, though there are only 4 such clusters in our sample. Above $5.2 \times 10^{14} M_{\odot}$ the fraction rises to $8/10 = 80 \pm 18\%$. If we include cRRs, these become $3/12 = 25 \pm 10\%$ and $8/12 = 67 \pm 16\%$, respectively.

It is already well-established that the occurrence of RHs drops significantly as cluster mass decreases (Cuciti et al. 2015, 2021). Our results suggest that the difference between the two populations of merging galaxy clusters could be explained by the mass-dependence of RH occurrence (see Cassano et al. 2023). However, since the cluster redshift also plays a significant role in RH occurrence, full comparison of the occur-

rence in relic-hosting clusters to all clusters in the LoTSS DR2 – PSZ2 sample requires restricting analysis to a relatively small redshift range. Due to the low numbers of RRs, and the correlation of the cluster mass with redshift (Fig. 1), even the most-populated redshift bin of Cassano et al. (2023) does not allow for statistical analysis. Larger surveys, with greater numbers of observed relics, will be required to test if the cluster mass can explain the differences between merging cluster populations. We expect that the number of RHs and relics in PSZ2 clusters should more than double by the completion of LoTSS (see Botteon et al. 2022), which should allow greater constraints to be set on the connection between RHs and relics.

4.5. Location and size of relics

Radio relics are typically found in cluster outskirts. Vazza et al. (2012) found that this could be explained by the increase in kinetic energy dissipated at the shocks with radius and the fact that relics propagating in the line of sight should be both rare and faint. In their study of simulated relics, they found that most should be located >800 kpc from the cluster centre. For reference, we plot a line at 800 kpc in Fig. 9 (top), which shows the distribution of our relic – cluster centre distances. In line with expectations, most ($25/28 = 89 \pm 19\%$, excluding PSZ2 G107.10+65.32) relics are located beyond this projected distance from the cluster centre, and none below 450 kpc. Additionally, only a few relics lie at very large distances from the cluster centre, in line with Vazza et al. (2012), who showed that the kinetic flux through a shock peaks around ~ 1 Mpc and subsequently decreases towards larger radii. When plotted instead as a fraction of the cluster R_{500} (Fig. 9, bottom), we see a similar picture, that is to say that all relics lie $>0.5R_{500}$ from the cluster centre, and more than half lie $>R_{500}$ ($15/28$). This is in line with simulations by Zhang et al. (2019), who argued that the steep gas density profiles in cluster outskirts $\gtrsim R_{500}$ create a “habitable zone” for long-lived, runaway merger shocks. The selection

³ PSZ2 G069.39+68.05 hosts a cRH, but we exclude it from occurrence calculations.

criteria used to define relics likely plays a role in the lack of relics at small radii. Since relics were classified as such by their location outside the bulk of ICM emission, our results may be biased towards larger cluster centre distances. However, relics located near the cluster centre are rare (e.g., Bonafede et al. 2012; Feretti et al. 2012, FdG14).

As in previous statistical studies of relics (van Weeren et al. 2009; Bonafede et al. 2012, FdG14), we find that relics further from their cluster centre are typically larger, that is to say that they have a larger LLS (see Fig. 8). We also find that a larger LLS tends to be associated with a larger downstream width. This suggests that shock surfaces expand as they propagate into lower-density environments. For comparison, we also plot the LLS- D_{RR-c} correlation of FdG14. We find that the slopes are very similar, despite the large difference in observing frequency. This shows that the LLS does not change much as we move to lower frequencies, which we might expect, since the line joining the most distant relic regions typically lies parallel to the shock front.

5. Conclusions

In this paper we have presented the first statistical sample of RRs observed at 150 MHz, systematically measuring the relic properties in a uniform manner. We used the LoTSS DR2 – PSZ2 sample of galaxy clusters (Botteon et al. 2022). Where available, archival X-ray data has been utilised to aid in source classification and cluster property measurements (full analysis of the sample in X-rays will follow in Zhang et al. 2023). Our main results are as follows:

- We find that RRs are relatively rare phenomena, even when moving to low frequencies. In the LoTSS DR2 – PSZ2 sample, $\sim 10\%$ of clusters host at least one relic. This is greater than at higher frequencies, however it is nonetheless much lower than predicted by simulations.
- We confirm the relationship between RRs and merging galaxy clusters. Radio relic-hosting clusters are among the most dynamically disturbed in the LoTSS DR2 – PSZ2 sample.
- We have revisited previous correlations of RR properties. We find a positive correlation between the RR power and the cluster mass ($p = 0.003$). We do however find evidence that cluster mass actually sets an upper limit on the power of a relic, rather than being a direct driver. We find a correlation between relic power and its LLS, though only when cRRs are included ($p = 0.029$). We also find a correlation between relic LLS and its radial distance from the cluster ($p = 0.002$) and as a fraction of cluster R_{500} ($p < 0.001$), that is to say that relics located further from the cluster centre tend to be larger.
- We have developed methods to measure the properties of a relic in a systematic and homogeneous way. In particular, we have introduced a statistical method of defining the relic downstream width as the median of the distribution of widths measured along the relic’s extent. Using this, we have shown that, even given optimistic downstream shock properties, the width of RRs in almost all cases is too large to be explained by only synchrotron and inverse Compton losses.
- We have compared the properties of the relic-hosting clusters in our sample which do, and do not, also host a RH. We do not find any evidence for the two populations being at different evolutionary stages, nor differences in the merging state of the host cluster. We find that the change in halo occur-

rence as a function of mass and redshift could go some way to explaining the discrepancy, but the sample is too small for conclusive evidence.

- We find that most relics lie in the cluster outskirts. $\sim 90\%$ of relics lie >800 kpc from their cluster centre, in line with cosmological simulations. All relics lie $>0.5R_{500}$ and more than half lie above R_{500} .

The low occurrence of RRs means that large samples are necessary to understand their statistical properties. Extrapolating from LoTSS DR2 to the full LoTSS survey, the number of detected relics in *Planck* PSZ2 clusters is expected to more than double (Botteon et al. 2022). This work will therefore be expanded in future, improving the constraints we can set on RR properties.

Acknowledgements. F.d.G. and M.B. acknowledge support from the Deutsche Forschungsgemeinschaft under Germany’s Excellence Strategy – EXC 2121 “Quantum Universe” – 390833306. A. Botteon acknowledges support from the ERC-StG DRANOEL n. 714245 and from the VIDI research programme with project number 639.042.729, which is financed by the Netherlands Organisation for Scientific Research (NWO). F.G., M.R., and R.C. acknowledge support from INAF mainstream project ‘Galaxy Clusters Science with LOFAR’ 1.05.01.86.05. A. Bonafede acknowledges support from ERC StG DRANOEL n. 714245 and MIUR FARE grant “SMS”. V.C. and G.D.G. acknowledge support from the Alexander von Humboldt Foundation. A.D. acknowledges support by the BMBF Verbundforschung under the grant 05A20STA. D.N.H. acknowledges support from the ERC through the grant ERC-StG DRANOEL n. 714245. K.R. acknowledges financial support from the ERC Starting Grant “MAGCOW” no. 714196. R.J.v.W. acknowledges support from the ERC Starting Grant ClusterWeb 804208. The Low Frequency Array, designed and constructed by ASTRON, has facilities in several countries, that are owned by various parties (each with their own funding sources), and that are collectively operated by the International LOFAR Telescope (ILT) foundation under a joint scientific policy. The Jülich LOFAR Long Term Archive and the German LOFAR network are both coordinated and operated by the Jülich Supercomputing Centre (JSC), and computing resources on the supercomputer JUWELS at JSC were provided by the Gauss Centre for Supercomputing e.V. (grant CHTB00) through the John von Neumann Institute for Computing (NIC). This research has made use of SAOImage DS9, developed by Smithsonian Astrophysical Observatory. This research has made use of NASA’s Astrophysics Data System.

References

- Akamatsu, H., & Kawahara, H. 2013, *PASJ*, 65, 16
 Akamatsu, H., Mizuno, M., Ota, N., et al. 2017, *A&A*, 600, A100
 Akritas, M. G., & Bershad, M. A. 1996, *ApJ*, 470, 706
 Araya-Melo, P. A., Aragón-Calvo, M. A., Brüggén, M., & Hoefl, M. 2012, *MNRAS*, 423, 2325
 Basu, K. 2012, *MNRAS*, 421, 112
 Blandford, R., & Eichler, D. 1987, *Phys. Rep.*, 154, 1
 Bonafede, A., Brüggén, M., van Weeren, R., et al. 2012, *MNRAS*, 426, 40
 Bonafede, A., Intema, H. T., Brüggén, M., et al. 2014, *ApJ*, 785, 1
 Bonafede, A., Cassano, R., Brüggén, M., et al. 2017, *MNRAS*, 470, 3465
 Botteon, A., Gastaldello, F., Brunetti, G., & Dallacasa, D. 2016a, *MNRAS*, 460, L84
 Botteon, A., Gastaldello, F., Brunetti, G., & Kale, R. 2016b, *MNRAS*, 463, 1534
 Botteon, A., Brunetti, G., Ryu, D., & Roh, S. 2020a, *A&A*, 634, A64
 Botteon, A., van Weeren, R. J., Brunetti, G., et al. 2020b, *MNRAS*, 499, 11
 Botteon, A., Cassano, R., van Weeren, R. J., et al. 2021, *ApJ*, 914, L29
 Botteon, A., Shimwell, T. W., Cassano, R., et al. 2022, *A&A*, 660, A78
 Bourdin, H., Mazzotta, P., Markevitch, M., Giacintucci, S., & Brunetti, G. 2013, *ApJ*, 486, 347
 Boxelaar, J. M., van Weeren, R. J., & Botteon, A. 2021, *Astron. Comput.*, 35, 100464
 Brüggén, M., & Vazza, F. 2020, *MNRAS*, 493, 2306
 Brunetti, G., & Jones, T. W. 2014, *Int. J. Mod. Phys. D*, 23, 1430007
 Brunetti, G., Cassano, R., Dolag, K., & Setti, G. 2009, *A&A*, 507, 661
 Bruno, L., Brunetti, G., Botteon, A., et al. 2023, *A&A*, 672, A41
 Cassano, R., & Brunetti, G. 2005, *MNRAS*, 357, 1313
 Cassano, R., Etori, S., Giacintucci, S., et al. 2010, *ApJ*, 721, 82
 Cassano, R., Etori, S., Brunetti, G., et al. 2013, *ApJ*, 777, 141
 Cassano, R., Brunetti, G., Giocoli, C., & Etori, S. 2016, *A&A*, 593, A81
 Cassano, R., Cuciti, V., Brunetti, G., et al. 2023, *A&A*, 672, A43
 Cuciti, V., Cassano, R., Brunetti, G., et al. 2015, *A&A*, 580, A97
 Cuciti, V., Cassano, R., Brunetti, G., et al. 2021, *A&A*, 647, 51

- Cuciti, V., Cassano, R., Sereno, M., et al. 2023, *A&A*, **680**, A30
- de Gasperin, F., van Weeren, R. J., Brüggen, M., et al. 2014, *MNRAS*, **444**, 3130
- de Gasperin, F., Intema, H. T., Shimwell, T. W., et al. 2017, *Sci. Adv.*, **3**, e1701634
- de Gasperin, F., Brunetti, G., Brüggen, M., et al. 2020, *A&A*, **642**, A85
- de Gasperin, F., Rudnick, L., Finoguenov, A., et al. 2022, *A&A*, **659**, A146
- Di Gennaro, G., van Weeren, R. J., Hoeft, M., et al. 2018, *ApJ*, **865**, 24
- Di Gennaro, G., van Weeren, R. J., Rudnick, L., et al. 2021, *ApJ*, **911**, 3
- Domínguez-Fernández, P., Brüggen, M., Vazza, F., et al. 2021, *MNRAS*, **500**, 795
- Donnert, J., Dolag, K., Brunetti, G., & Cassano, R. 2013, *MNRAS*, **429**, 3564
- Dwarakanath, K. S., Parekh, V., Kale, R., & George, L. T. 2018, *MNRAS*, **477**, 957
- Eckert, D., Jauzac, M., Vazza, F., et al. 2016, *MNRAS*, **461**, 1302
- Enßlin, T. A., Biermann, P. L., Klein, U., & Kohle, S. 1998, *A&A*, **332**, 395
- Feretti, L., Giovannini, G., Govoni, F., & Murgia, M. 2012, *A&ARv*, **20**, 1
- Fermi, E. 1949, *Phys. Rev.*, **75**, 1169
- Finner, K., Jee, M. J., Golovich, N., et al. 2017, *ApJ*, **851**, 46
- Finoguenov, A., Sarazin, C. L., Nakazawa, K., Wik, D. R., & Clarke, T. E. 2010, *ApJ*, **715**, 1143
- Fujita, Y., Akamatsu, H., & Kimura, S. S. 2016, *PASJ*, **68**, 34
- George, L. T., Dwarakanath, K. S., Johnston-Hollitt, M., et al. 2015, *MNRAS*, **451**, 4207
- Golovich, N., Dawson, W. A., Wittman, D. M., et al. 2019, *ApJ*, **240**, 39
- Hoang, D. N., Brüggen, M., Botteon, A., et al. 2022, *A&A*, **665**, A60
- Hoeft, M., & Brüggen, M. 2007, *MNRAS*, **375**, 77
- Jee, M. J., Dawson, W. A., Stroe, A., et al. 2016, *ApJ*, **817**, 179
- Jones, A., de Gasperin, F., Cuciti, V., et al. 2021, *MNRAS*, **505**, 4762
- Kale, R., Dwarakanath, K. S., Bagchi, J., & Paul, S. 2012, *MNRAS*, **426**, 1204
- Kale, R., Venturi, T., Giacintucci, S., et al. 2015, *A&A*, **579**, A92
- Kang, H. 2016, *J. Korean Astron. Soci.*, **49**, 145
- Kang, H., & Ryu, D. 2011, *ApJ*, **734**, 18
- Kang, H., Ryu, D., & Jones, T. W. 2012, *ApJ*, **756**, 97
- Kang, H., Ryu, D., & Jones, T. W. 2017, *ApJ*, **840**, 42
- Liang, H., Hunstead, R. W., Birkinshaw, M., & Andreani, P. 2000, *ApJ*, **544**, 686
- Lovisari, L., Schellenberger, G., Sereno, M., et al. 2020, *ApJ*, **892**, 102
- Mandal, S., Intema, H. T., van Weeren, R. J., et al. 2020, *A&A*, **634**, A4
- Markevitch, M., Gonzalez, A. H., David, L., et al. 2002, *ApJ*, **567**, 27
- Markevitch, M., Govoni, F., Brunetti, G., & Jerius, D. 2005, *ApJ*, **627**, 733
- Mohr, J. J., Fabricant, D. G., & Geller, M. J. 1993, *ApJ*, **413**, 492
- Nuza, S. E., Hoeft, M., van Weeren, R. J., Gottlöber, S., & Yepes, G. 2012, *MNRAS*, **420**, 2006
- Nuza, S. E., Gelszinnis, J., Hoeft, M., & Yepes, G. 2017, *MNRAS*, **470**, 240
- Ogrea, G. A., & Brüggen, M. 2013, *MNRAS*, **433**, 1701
- Ogrea, G. A., Brüggen, M., Röttgering, H., et al. 2013, *MNRAS*, **429**, 2617
- Piffaretti, R., Arnaud, M., Pratt, G. W., Pointecouteau, E., & Melin, J.-B. 2011, *A&A*, **534**, A109
- Pinzke, A., Oh, S. P., & Pfrommer, C. 2013, *MNRAS*, **435**, 1061
- Planck Collaboration XXIX. 2014, *A&A*, **571**, A29
- Planck Collaboration XXVII. 2016, *A&A*, **594**, A27
- Poole, G. B., Fardal, M. A., Babul, A., et al. 2006, *MNRAS*, **373**, 881
- Pratt, G. W., Croston, J. H., Arnaud, M., & Böhringer, H. 2009, *A&A*, **498**, 361
- Rajpurohit, K., Vazza, F., Hoeft, M., et al. 2020, *A&A*, **642**, L13
- Rajpurohit, K., van Weeren, R. J., Hoeft, M., et al. 2022, *ApJ*, **927**, 80
- Santos, J. S., Rosati, P., Tozzi, P., et al. 2008, *A&A*, **483**, 35
- Shimwell, T. W., Markevitch, M., Brown, S., et al. 2015, *MNRAS*, **449**, 1486
- Shimwell, T. W., Hardcastle, M. J., Tasse, C., et al. 2022, *A&A*, **659**, A1
- Tasse, C., Shimwell, T., Hardcastle, M. J., et al. 2021, *A&A*, **648**, A1
- Urdampilleta, I., Akamatsu, H., Mernier, F., et al. 2018, *A&A*, **618**, A74
- van Weeren, R. J., Röttgering, H. J. A., Brüggen, M., & Cohen, A. 2009, *A&A*, **508**, 75
- van Weeren, R. J., Brüggen, M., Röttgering, H. J., & Hoeft, M. 2011, *MNRAS*, **418**, 230
- van Weeren, R. J., Andrade-Santos, F., Dawson, W. A., et al. 2017, *Nat. Astron.*, **1**, 0005
- van Weeren, R. J., de Gasperin, F., Akamatsu, H., et al. 2019, *Space Sci. Rev.*, **215**, 16
- van Weeren, R. J., Shimwell, T. W., Botteon, A., et al. 2021, *A&A*, **651**, A115
- Vazza, F., Brüggen, M., van Weeren, R., et al. 2012, *MNRAS*, **421**, 1868
- Wittor, D., Ettori, S., Vazza, F., et al. 2021, *MNRAS*, **506**, 396
- Zhang, C., Churazov, E., Forman, W. R., & Lyskova, N. 2019, *MNRAS*, **488**, 5259
- Zhang, X., Simionescu, A., Gastaldello, F., et al. 2023, *A&A*, **672**, A42

Appendix A: Radio relic image gallery

Fig. A.1 shows LOFAR 50 kpc-taper, discrete source-subtracted images of all RRs in the LoTSS DR2 - PSZ2 galaxy cluster sample. The images are taken from Botteon et al. (2022) and are also available on the project website⁴. All images are centred on the PSZ2 cluster coordinates, except PSZ2 G165.46+66.15 which is centred on the X-ray centroid. The RRs in PSZ2 G089.52+62.34, PSZ2 G091.79-27.00, and PSZ2 G165.46+66.15 were not fully covered by the images, so we have re-imaged these clusters. The black circle denotes the cluster R_{500} , centred on the PSZ2 coordinates. Each image includes a 1 Mpc scalebar and information on the cluster mass, redshift, and image rms. The blue ellipse shows

the image beam size. White crosses denote the coordinates used as the relic positions (see Sec. 2.2).

Fig. A.2 shows the same radio images as white contours, overlaid on *Chandra/XMM-Newton* X-ray images. The instrument used is shown in the image title. The radio contours are spaced by factor of 2, starting at $2\sigma_{rms}$. PSZ2 G089.52+62.34, PSZ2 G091.79-27.00, and PSZ2 G165.46+66.15 are again re-imaged. The R_{500} , centred on the PSZ2 coordinates, is shown as a white circle. The position of the X-ray centroids, used as the cluster centres in our analysis, are denoted by black crosses. We note that, for PSZ2 G107.10+65.32, only the X-ray centroid of the S subcluster is plotted. All other information is as in Fig. A.1.

⁴ https://lofar-surveys.org/planck_dr2.html

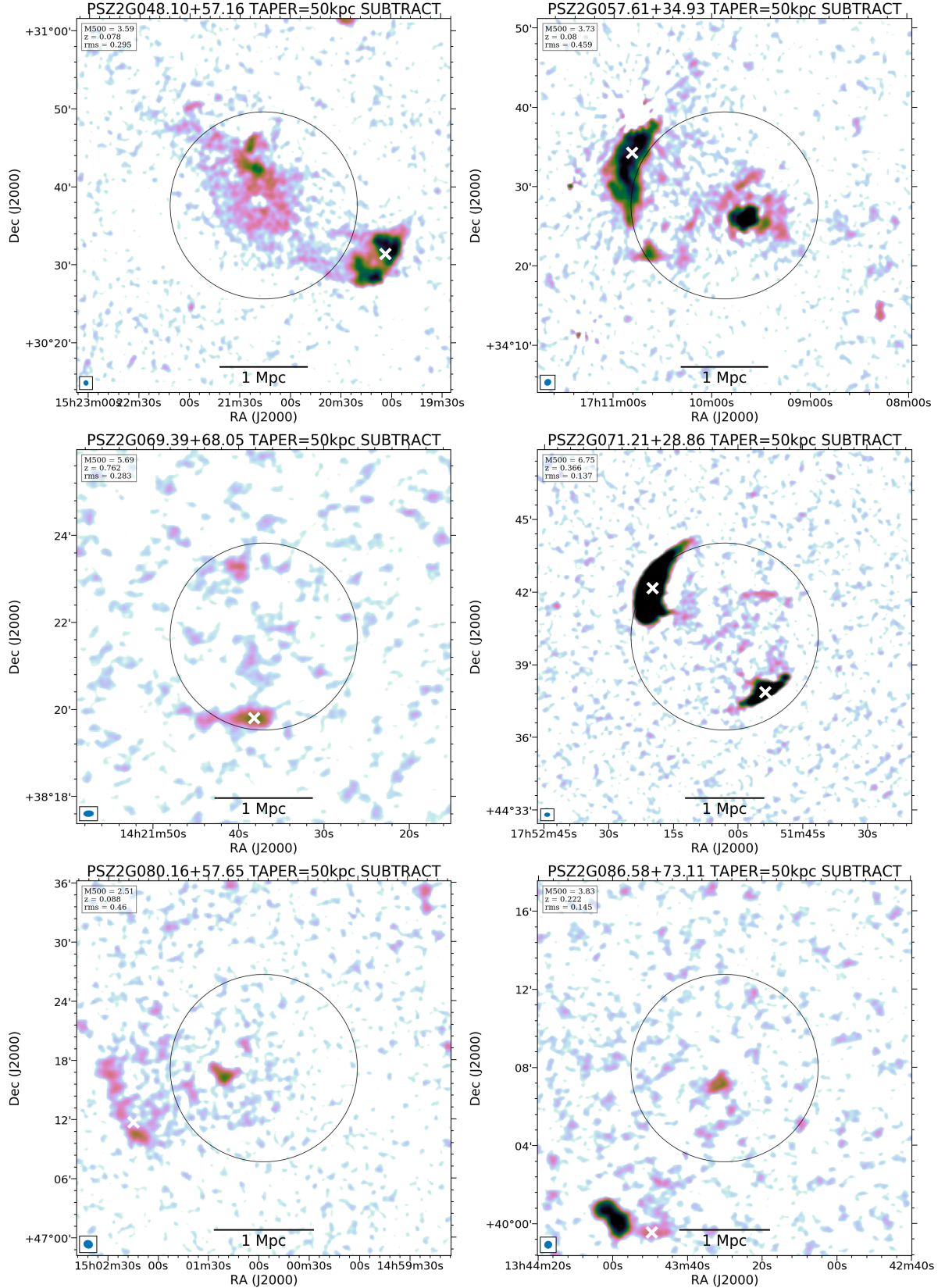


Fig. A.1. LOFAR 50kpc-taper, discrete source-subtracted images of the RRs in the LoTSS DR2 - PSZ2 sample, from [Botteon et al. \(2022\)](#). The images and R_{500} (black circles) are centred on the PSZ2 coordinate. The image of PSZ2 G165.46+66.15 is centred on the X-ray centroid. PSZ2 G089.52+62.34, PSZ2 G091.79-27.00, and PSZ2 G165.46+66.15 have been re-imaged. A scalebar, denoting 1 Mpc, is shown in black. The beam is shown in the bottom-left corner, and the mass (M_{500} , in units of $10^{14} M_{\odot}$), redshift (z), and image noise (rms, in units of mJy beam^{-1}) are reported in the top-left corner. White crosses mark the location of the relics, as used throughout the paper (see Sec. 2.2 for a description of their calculation).

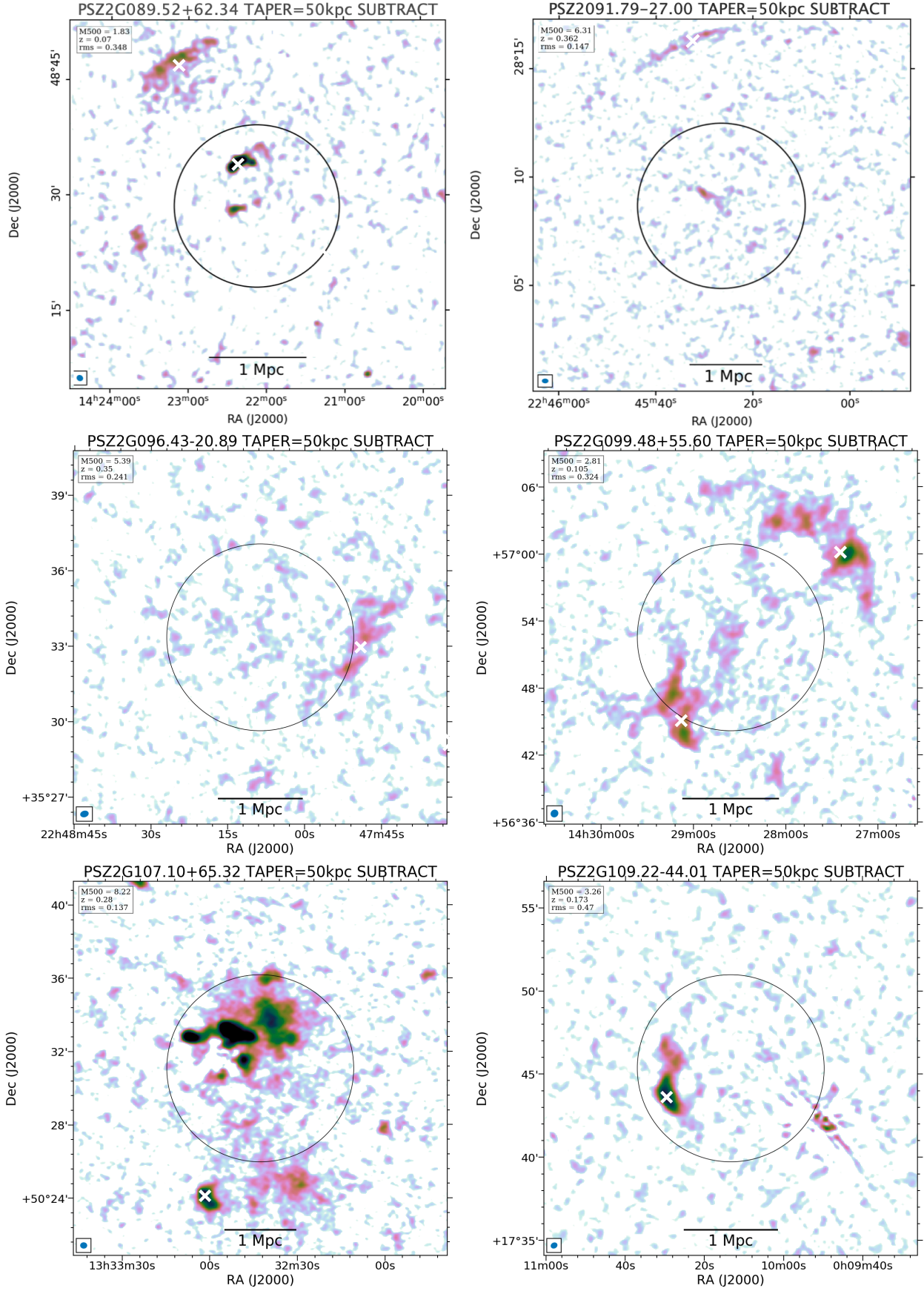


Fig. A.1. continued.

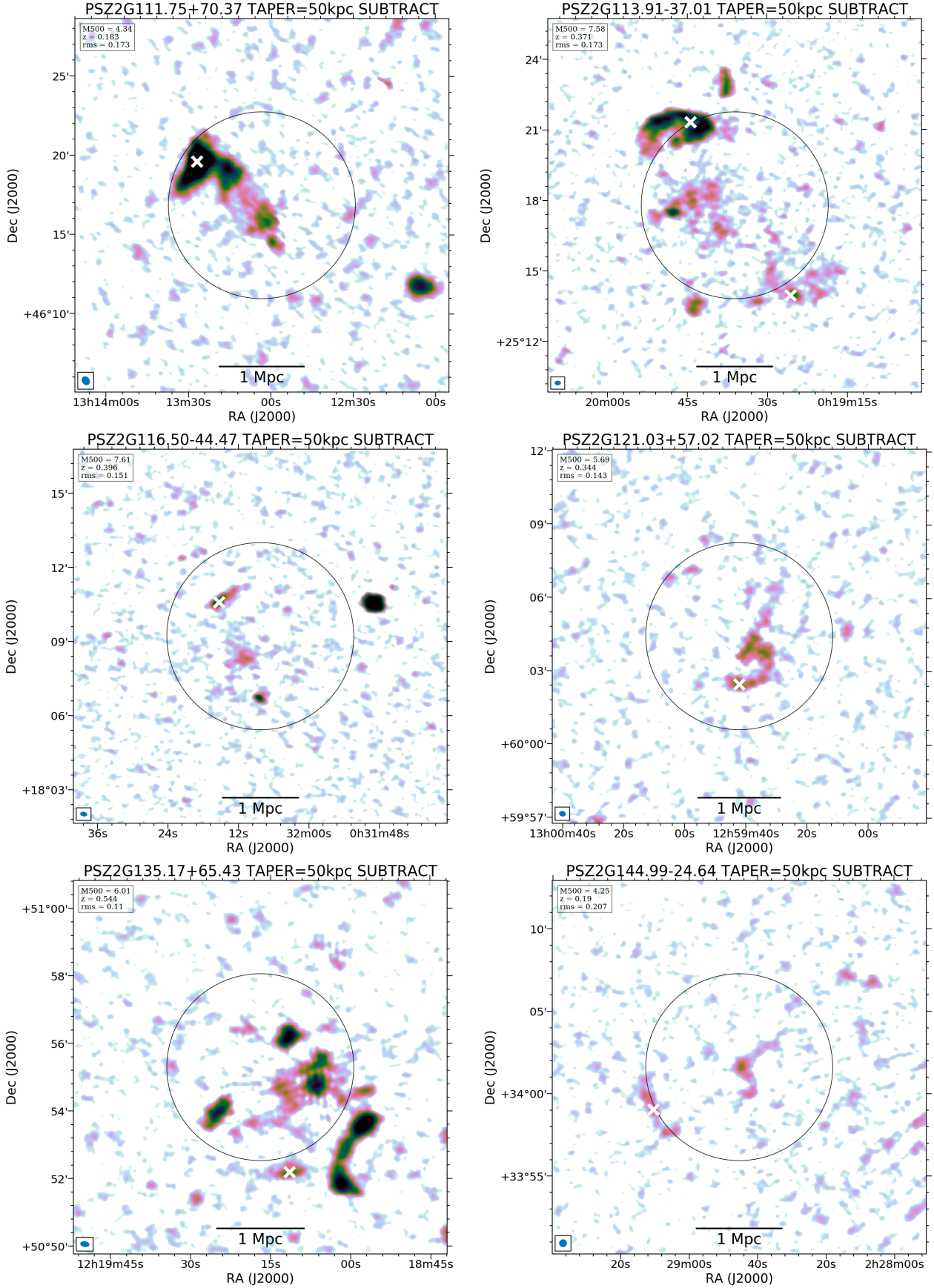


Fig. A.1. continued.

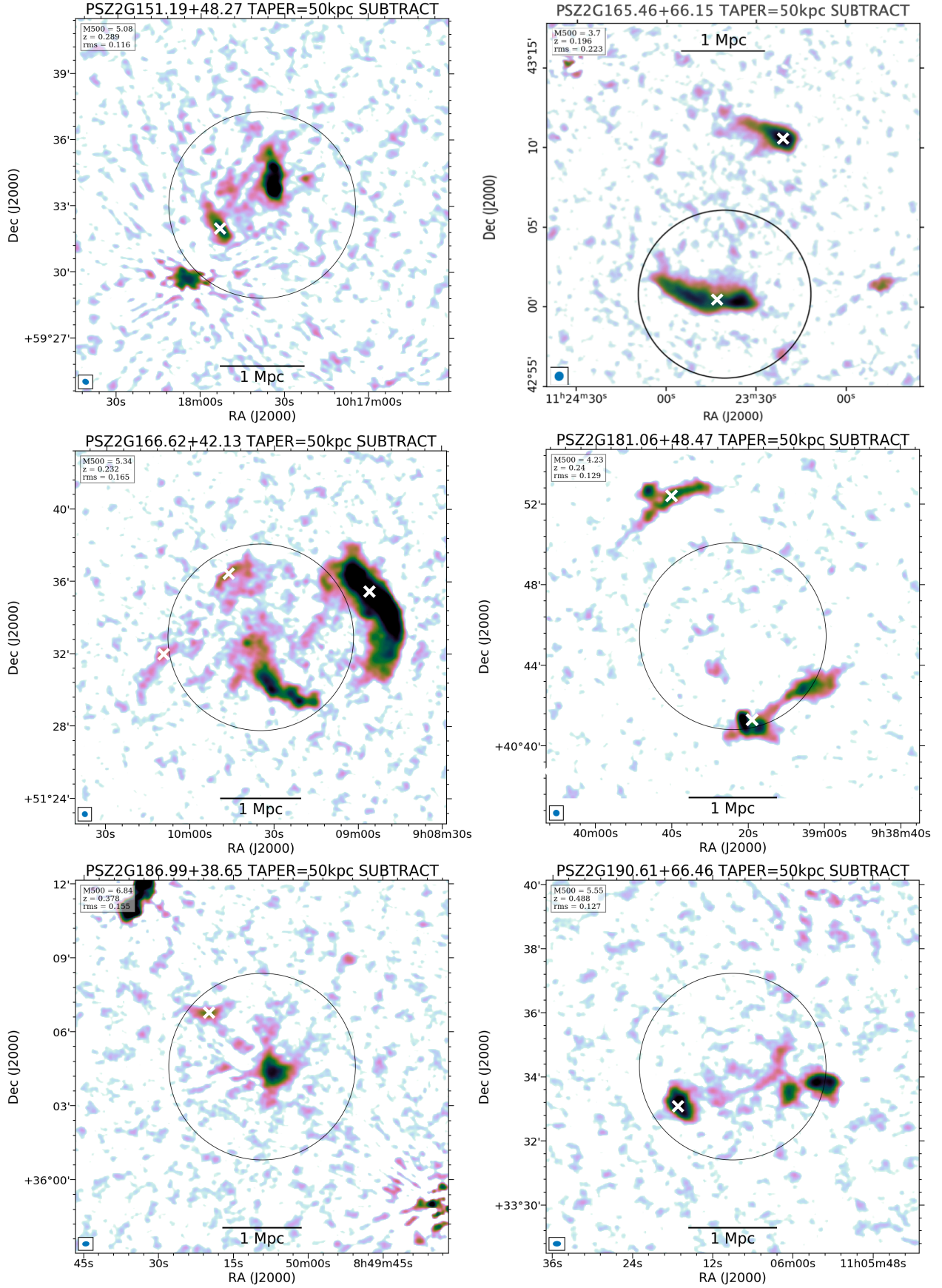


Fig. A.1. continued.

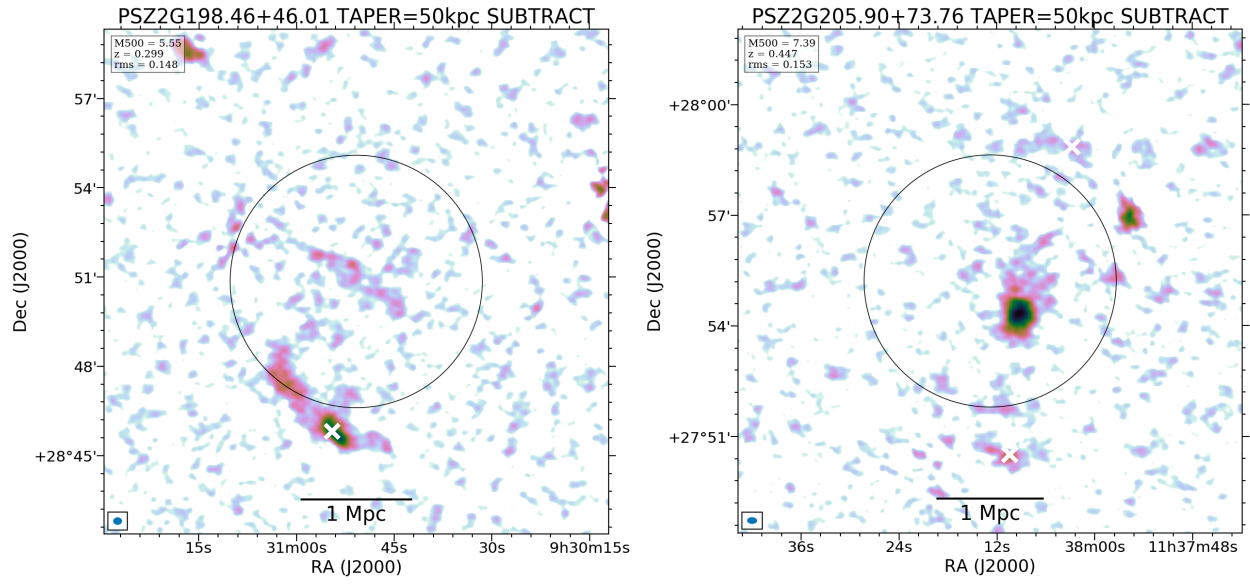


Fig. A.1. continued.

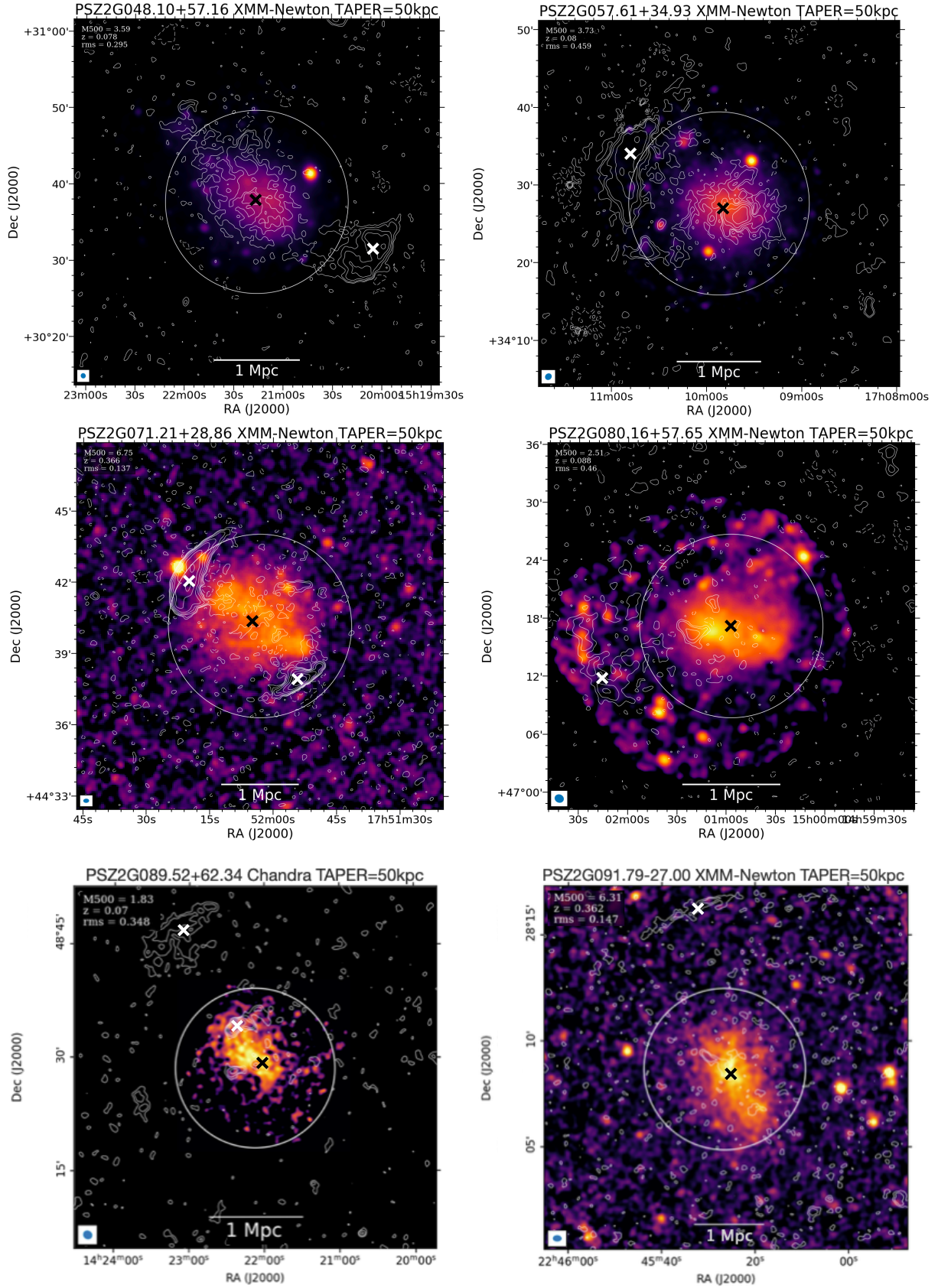


Fig. A.2. *Chandra/XMM-Newton* images of the relic-hosting clusters in our sample. The white contours show the corresponding radio images (Fig. A.1) spaced by a factor of 2, starting at $2\sigma_{rms}$. Black crosses mark the position of the X-ray centroid. We note that, for PSZ2 G107.10+65.32, only the X-ray centroid of the S subcluster is plotted. All other information is as in Fig. A.1.

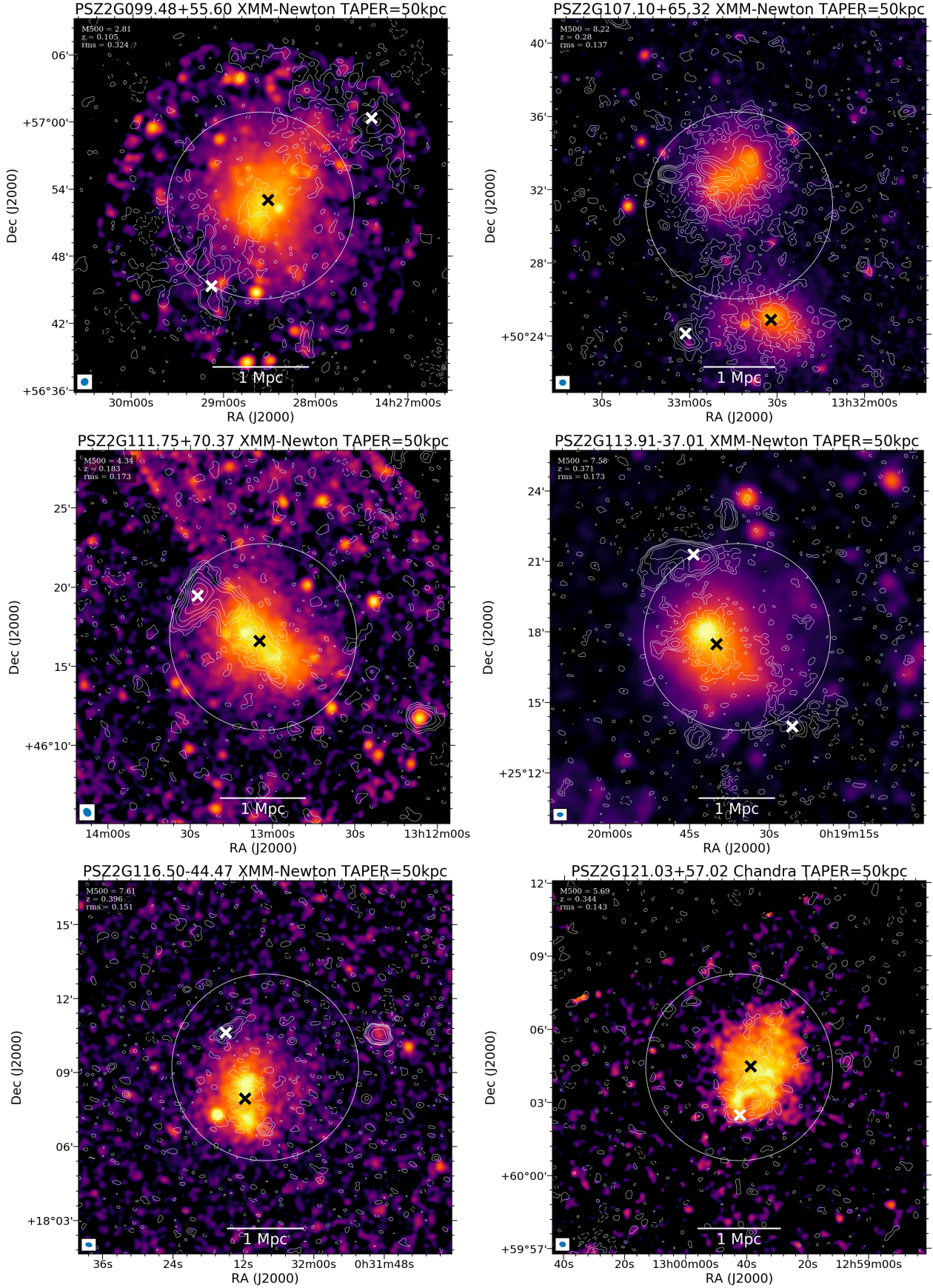


Fig. A.2. continued.

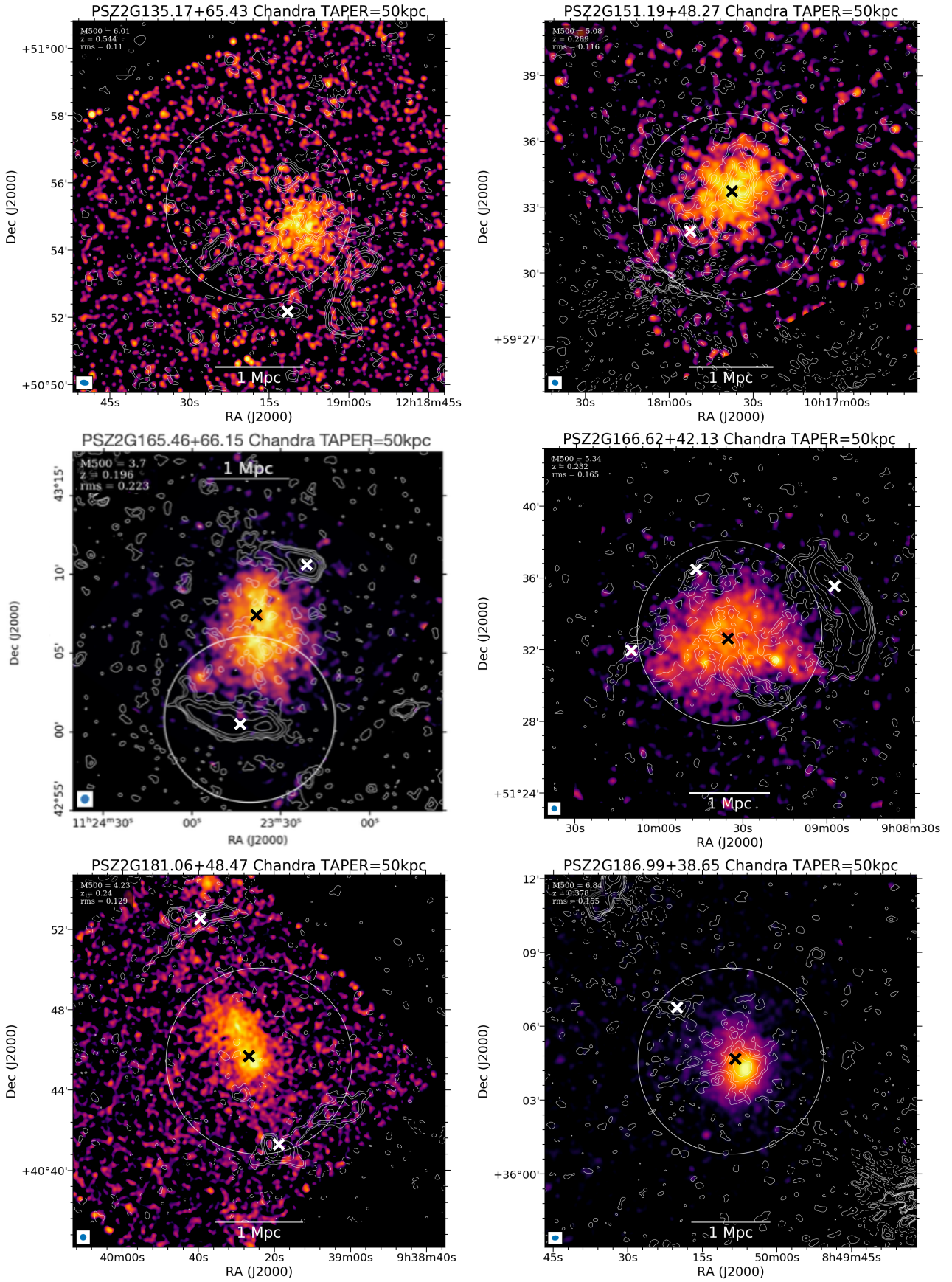


Fig. A.2. continued.

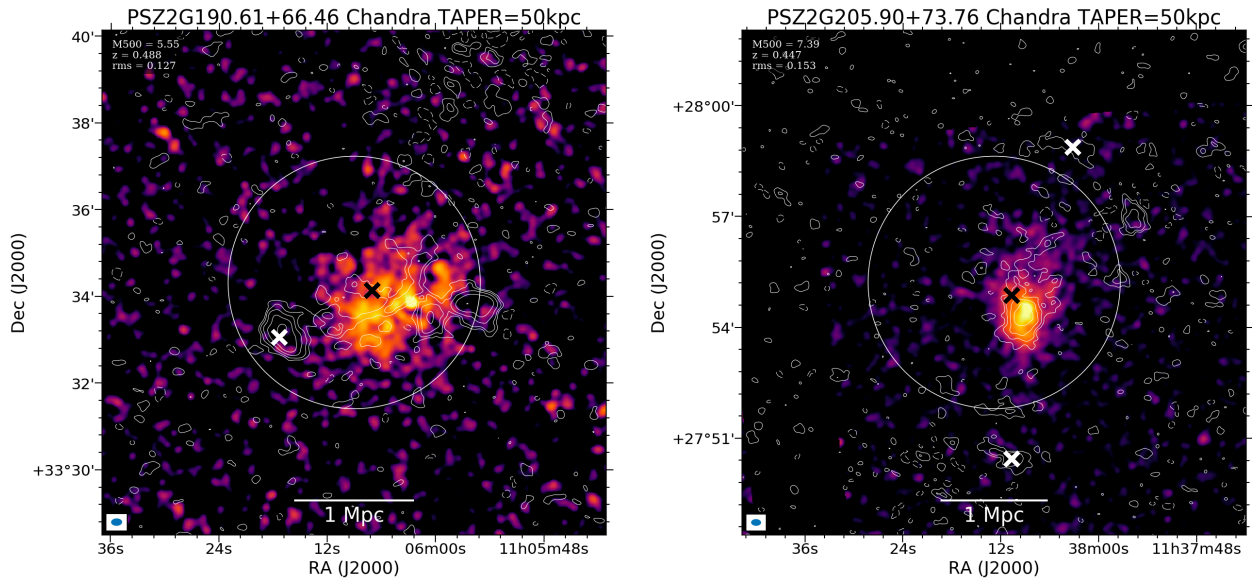


Fig. A.2. continued.

Appendix B: Comparison with FdG14 powers

In Fig. 6 we compare the power vs. mass scaling relations of the relics in this sample (150 MHz) and those used by FdG14 (1.4 GHz). To make a completely fair comparison, the cosmology used to calculate the relic powers should be the same. In Fig. B.1 we reproduce Fig. 6 (top) with the relic powers from our sample recomputed with the same cosmology as FdG14 (Λ CDM cosmology with $\Omega_\Lambda = 0.73$, $\Omega_m = 0.27$, and $H_0 = 71 \text{ km s}^{-1} \text{ Mpc}^{-1}$), since the scaling relation in FdG14 was calculated with this cosmology. The slope and intercept (orthogonal fit) of the line of best fit for the recomputed powers are $B = 5.84 \pm 1.31$ and $A = -60.74 \pm 19.27$.

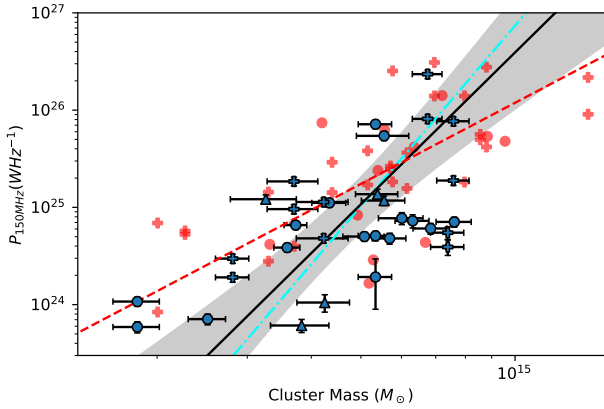


Fig. B.1. Same as Fig. 6 (top) but the relic powers from the DR2 sample have been recomputed using the cosmology used by FdG14.

Appendix C: Fitting methods

The slope and intercept obtained when fitting a regression line depends on the fitting method (see Tab. 2). In this paper we report the parameters for four different methods: orthogonal; Y|X; X|Y and the bisector of Y|X and X|Y. In Fig. C.1 we show the regression line (confirmed relics only) for each fitting method.

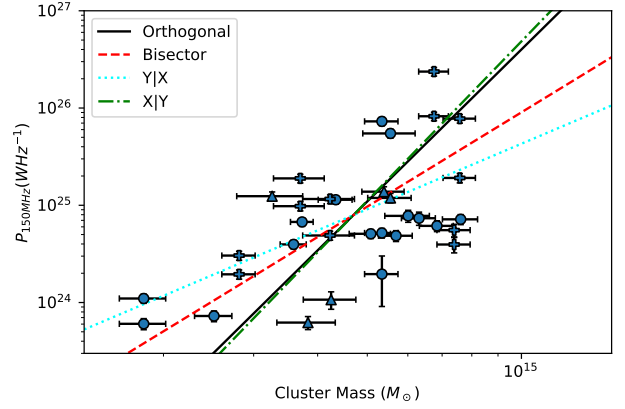


Fig. C.1. Relic power vs. cluster mass for confirmed relics only. The regression lines are shown for all four fitting methods.